Energy Conversion and Management 312 (2024) 118562

Contents lists available at ScienceDirect

Energy Conversion and Management

journal homepage: www.elsevier.com/locate/enconman

Research Paper

Advancing autonomy of chemical kinetics based multizone models for reactivity controlled compression ignition engines

Aneesh Vasudev [a], Alireza Kakoee [a], Martin Axelsson [b], Hamidreza Maleki Almani [c], Jari Hyvönen [b], Maciej Mikulski [a,*]

[a] Efficient Powertrain Solutions, School of Technology and Innovation, University of Vaasa, Wolffintie 34, FI-65200 Vaasa, Finland
[b] Wärtsilä Finland OY, FI-65170 Vaasa, Finland
[c] Department of Mathematics and Statistics, School of Technology and Innovations, University of Vaasa, Wolffintie 34, FI-65200 Vaasa, Finland

ARTICLE INFO

Keywords:
RCCI
Quasi-dimensional model
Engine rapid prototyping
Emissions prediction

ABSTRACT

Model-based calibration of high-efficient reactivity controlled compression ignition (RCCI) engines popularly rely on chemical-kinetics based multizone models (MZM) for predictive, performance-oriented simulations. These models however, employ heuristic approaches to capture the critical phenomena of direct-injected fuel stratification and interzonal mixing, which limit their utility. These issues are presently addressed by (i) developing a semi-predictive fuel stratification sub-model; and (ii) implementing in-cylinder mixing based on the turbulence energy cascade mechanism. The simulations are parameterized to the latest line-up of Wärtsilä's 20DF marine engines, with model calibration additionally supported by CFD results on this target cylinder geometry. Operating on natural gas and diesel fuelled RCCI, validation against the engine measurements reveals correct sensitivities to all combustion control parameters including injection timing and duration, and boost pressure. The MZM's prediction accuracy is within 1.5°CA for combustion phasing, and all synthetic performance indicators, derived from pressure trace, are within 5% error. Additionally, the model reproduces the traces of mass averaged turbulent kinetic energy and turbulent viscosity within a relative root mean square error of 10% with respect to detailed CFD results. The realistic fuel distribution and improved interzonal mixing allows for accurate predictions of nitrogen oxides and hydrocarbon emissions in-line with state-of-the-art MZMs. With an average simulation time below 4 min per cycle, makes the improved MZM viable for rapid prototyping next-generation RCCI engines.

1. Introduction

Combustion engines are indispensable in marine transportation amid the shift to a carbon–neutral future. The International Maritime Organization (IMO) recognises that the vast scale of maritime operations and limited infrastructure for alternative technologies mean that the transition to clean energy must be gradual. Combustion engines provide continuity of efficient, long-haul shipping during ongoing development of environmental impact mitigation measures, such as emission reduction, combustion optimisation and sustainable fuel solutions.

Reactivity-controlled compression ignition (RCCI) has emerged as a promising concept among state-of-the-art combustion technologies. Enabled by low temperature combustion (LTC) technology, RCCI offers twin benefits of improved thermal efficiency and reduced emissions [1]. As a dual-fuel concept, it facilitates greater control over combustion performance and is higher on the technology readiness level ladder [2] than other LTC strategies. It is fuel-flexible, with demonstrators employing gasoline [3,4], alcohols [5,6], methane [7,8] as the low reactivity fuel (LRF) and mineral-diesel [7], bio-diesel [5,6] as high reactivity fuel (HRF). Natural gas (NG) – diesel RCCI has shown direct engine-out emissions below EURO-VI standard, while improvement by 2–4 percentage points (pp) in indicated thermal efficiency over the conventional heavy-duty diesel operation [2,7].

Despite improved combustion control, RCCI is nevertheless driven by chemical kinetics [1]. Consequently, the parameters for solely controlling combustion phasing include injection timing, fuel blending, IVC thermal management, and reactivity stratification. Furthermore, RCCI operation is characterised by high pressure rise rate (PRR) and peak cylinder pressure (P_{max}) levels [1] which limit high-load operation. Under part- and low-load conditions, unburnt hydrocarbons (UHC) and CO emissions become an issue [9].

* Corresponding author.
E-mail addresses: aneesh.vasudev@uwasa.fi (A. Vasudev), maciej.mikulski@uwasa.fi (M. Mikulski).

https://doi.org/10.1016/j.enconman.2024.118562
Received 6 March 2024; Received in revised form 29 April 2024; Accepted 14 May 2024
Available online 18 May 2024

Nomenclature:

Abbreviations

BR	blend ratio
CAX	Crank angle corresponding to X% energy released
CFD	computational fluid dynamics
CHR	cumulative heat release
HCCI	homogeneous charge compression ignition
HRF	high reactivity fuel
HRR	heat release rate
iEGR	internal exhaust gas recirculation
IMEP	indicated mean effective pressure
IMEP720	net indicated mean effective pressure
IMO	International Maritime Organization
IVC	intake valve closing
LRF	low reactivity fuel
LTC	low temperature combustion
MPRR	maximum pressure rise rate
MZM	multizone model
NG	natural gas
NHR	net heat released
NO_X	oxides of nitrogen
PCCI	premixed charge compression ignition
pp	percentage points
PRR	pressure rise rate
RCCI	reactivity controlled compression ignition
RMSE	root mean square error
SE	standard error
SOC	start of combustion
SOI	start of injection
TDC	top dead centre
TDR	turbulent dissipation rate
TKE	turbulent kinetic energy
TKV	turbulent kinematic viscosity
UHC	unburnt hydrocarbons
UVATZ	University of Vaasa Advanced Thermo-kinetic multizone model

Symbols

°CA	crank angle degree
$\mathfrak{D}$	mass diffusion coefficient
m	mass
k	turbulent kinetic energy
P	pressure
Pr	Prandtl number
Q	heat
R_u	universal gas constant
Sc	Schmidt number
T	temperature
V	volume
w	zone thickness
ε	turbulent dissipation rate
ζ	multizone model tuning parameter
ϑ	kinematic viscosity
λ	air–fuel equivalence ratio
Λ	thermal conductivity
ρ	density

Subscripts

avg	average
cyl	cylinder
i	species index
iman	intake manifold
max	max
t	turbulent
∇	gradient

This translates to an immense calibration problem. A conventional full-factorial, data-driven approach to engine controller development and system optimisation entails a search space that scales with the exponent of 10^x. To this end, a model-based framework which employs predictive yet computationally light simulation tools is an efficient means to overcome the challenge. Quasi-dimensional models are physics-based approaches that bridge the gap between high-fidelity models such as CFD and data-driven or empirical approaches. In the context of LTC, these approaches are commonly referred to as multizone models (MZM), and are chemical-kinetics oriented while sacrificing fidelity on in-cylinder fluid physics.

One of the earliest works on multizone models applied to RCCI combustion is by Egüz et al. [10]. This was parameterised to a gasoline-diesel heavy-duty engine. The model comprised of 10 cylinder-shaped zones arranged annularly, with each zone exchanging heat and chemical composition with its immediate neighbours in order to reflect in-cylinder mixing. This flow was simplified to follow the diffusion mechanism, with the diffusion coefficient being a tuneable (case-dependent) multiplier on molecular diffusivity. Diesel injection was simplified to admitting fuel vapour at SOI across the zones, according to an imposed stratification profile. The stratification profiles were derived by processing CFD results of the injection process into a 1D fuel distribution across the zones, and mapped according to different injection timings (SOI). Validation was based mainly on the pressure trace and heat release profiles, for sweeps of diesel SOI and blend fractions of diesel-gasoline. The model was able to predict trends in combustion performance indicators, with absolute error for example in combustion phasing (CA50) within 5°CA.

This type of MZM is referred to as *onion-skin* and our earlier review work [11] expounds its use regards to setup, accuracy and applications. Egüz's model served as a foundation for a large number of works on RCCI multizone modelling from the group of Technical University of Eindhoven and TNO, where the approach has been extensively validated [2,12–17]. This group used it to study variable valve strategies [16,17], low reactivity fuel stratification [13], controller development [12,14,15] and engine optimisation [2]. Their MZM development started with the work of Bekdemir et al. [12] using Cantera-Matlab as a platform, with improvements in postprocessing to filter the jagged pressure trace – a characteristic of MZM in general. Mikulski and Bekdemir [13] adopted a more sophisticated 13 zone configuration, including a predictive wall-temperature solver for heat loss, and a plenum (gas-exchange) model for determining the state at intake valve closing (IVC). Accuracy was improved, with absolute combustion phasing error to 3°CA. Validation in both works [12,13] was performed against a NG-diesel RCCI heavy-duty engine. Emissions results of oxides of nitrogen (NO_X), CH_4, and CO followed trends of measurements. Work by Mikulski et al. [2] on marine engine optimisation was based on the aforementioned RCCI MZM, but also included an offline GT-Power air-path model for full cycle simulations. It is worth mentioning that simulation speed was around 30 min per cycle with a reaction mechanism consisting of 65 species and 354 reactions.

Lashkarpour et al. [18] constructed an onion-skin model with 11 zones including a boundary layer zone encasing all other zones, and a dedicated crevice zone, fixed to 3 % of clearance volume. Interzonal mass transfer occurs by virtue of pressure difference between neighbouring zones. Interzonal heat transfer, which also extends from the outermost zone to the cylinder walls, is based on the diffusion mechanism, and includes a predictive turbulence model [19] to determine the

magnitude of the diffusivity. Stratification of high-reactivity fuel across the zones was determined from CFD results for each operating point. Validation was performed against a NG-diesel RCCI engine, where their MZM demonstrated a 2.2°CA error in peak pressure position. Emissions were predicted well, with average error in NO_X estimate of 30 %; UHC estimation within 24.5 %; and CO within 5.5 %.

De Bellis et al. [20] recently developed a sophisticated onion-skin MZM with tabulated chemistry for accelerated simulations. Their approach also included a flame propagation model to predict both the RCCI and conventional dual-fuel combustion regimes. The combustion chamber volume was divided into a single burned zone and the unburned gas apportioned among 80 annularly arranged cylindrical zones. Interzonal heat transfer follows turbulent diffusion, as in the previous approach, while mass transfer is not modelled. HRF stratification is applied across the zones based on inference from CFD results, similar to Egüz et al. [10]. For open-cycle simulations, they coupled their MZM with GT-Power for 1-D air-path modelling. Their modelling framework was validated against a Wärtsilä 310 mm-bore, single-cylinder engine, over a wide dataset with 26 operating points. Their model predicted position of P_{max} within ± 2°CA, emissions within 35 % error margin and performance indicators within 5 % margins.

Although other approaches, such as spray-MZM [21] and stochastic reactor models [22] exist, onion-skin approaches have remained popular tools by far for simulating chemical-kinetics driven LTC concepts [11]. As such, the authors of the present work recently developed an onion-skin MZM [23] capable of simulations within three minutes (on single core), at an accuracy of 5 % to measurements. This 12 zone model applies the Yang and Martin approach [19] for turbulence-based interzonal heat and mass transfer. The MZM was later [24] coupled to a 1D air- and fuel-path model in GT-Power, with the objective of improved autonomy via better estimation of the IVC thermodynamic state. In both instances, the approach was validated on a 310 mm-bore, NG-diesel RCCI marine engine.

Despite their virtues in predictive, performance-oriented simulations, two potential improvements have been identified for onion-skin MZM. The first pertains to the in-cylinder stratification of direct-injected HRF, which among all identified MZM, has been modelled mainly as a heuristic approach (e.g. [20]) requiring case dependent tuning or an extensive calibration dataset. Although works like [10] mention that the approach was derived from CFD spray studies, they reveal little to no information on the methodology. On the other hand, the framework of Lashkarpour et al. [18] directly couples their MZM to a CFD model to obtain HRF stratification, which still restricts the MZM's autonomy. The second improvement point relates to the modelling of turbulent flow on mixing in terms of interzonal heat and mass transfer. This has been modelled as a simple scalar constant [10] or quasi-physical methodology, i.e., Yang and Martin approach [19]. The latter still limits predictivity because it is based on thermodynamic properties, thus, unable to reflect changes in mixing due to valve flow, fuel injection or cylinder geometry.

Based on these identified drawbacks, the present study aims to build upon the autonomy of the author's previously developed MZM [23] for NG-diesel RCCI engines by (i) implementing a predictive approach for HRF stratification. The zone-wise HRF distribution profile is obtained from a response surface approach that is setup based on data from CFD simulations, of the most influential parameters, on the target engine geometry. (ii) improve predictivity of interzonal-mixing by means of a physics-based 0D turbulence model, which tracks the histories of in-cylinder flow and turbulence quantities. This is calibrated and validated from CFD flow simulations. (iii) explore predictivity of NO_X and unburnt hydrocarbon emissions. Although challenging, the inherent features of the MZM, i.e., interzonal flows and chemical-kinetics, already allows trend-wise emission predictions. All three objectives are to be achieved without significant detriment to simulation speed. The target accuracy of performance indicators is under 5 % relative error, and that for emission is 35 %.

The paper's methodology section first describes the research engine platform, followed by the RCCI multizone combustion model, including governing assumptions and simulation methodology. Then comes a description of the CFD model: this is only brief because the paper's focus is MZM development. The final part of methodology section elaborates on the approach for predictive HRF stratification, including simulation and validation conditions. The results section begins with an illustration of the baseline MZM performance. The features of improved autonomy are demonstrated with the 0D-turbulence model validation, followed by the approach for predictive HRF stratification. After discussion of the emissions prediction, the section concludes with a compilation of model improvements. The paper's final section is devoted to key-takeaways and outlook.

2. Methodology

Simulation of NG-diesel RCCI combustion in this study is conducted based on University of Vaasa Advanced Thermo-kinetic multi-zone model (UVATZ) recently introduced [23] by the authors. To aid in the development of UVATZ in accordance with the established targets, CFD simulations are employed. As such, the objective for the CFD simulations is to deliver phenomenological insight regarding the processes of HRF spray and bulk in-cylinder turbulence. Validation of both UVATZ and the CFD model for supplementary simulations are based on RCCI measurement data from a full-metal research engine representing a Wärtsilä 20DF medium-speed marine engine line-up.

2.1. The research object and source of validation data

The geometrical and boundary data for the identification, calibration and validation of the modelling toolchain concerned in this study comes from a prototype RCCI research engine at Wärtsilä laboratories in Vaasa, Finland. The 6L20CRDF research engine is based on the Wärtsilä 20 platform with an inline six-cylinders dual fuel configuration. Everything except crankshaft and connecting rods are modified for fast and effective research activities by increasing flexibility and capability of upgrade to the latest technologies. Table 1 summarises the specifications of the research engine during the test campaign.

Speedgoat / CANape Rapid control prototyping is used for development of automation and control functionality. The engine has fully variable electrohydraulic valve actuation with full freedom in both valve lift and timing. It has two-stage turbocharging in series configuration. Centrally mounted, state-of-the-art, single-needle injectors handle direct injection of high-reactivity pilot fuel as well as supplying the full diesel quantity in diesel mode. There is multi-point gas injection upstream of the intake valves, through a low-pressure solenoid valve. NG with a methane number of about 80, paired with light fuel oil (LFO) as the high-reactive fuel, were used in the test campaign. In RCCI mode, the LFO was

Table 1
Specification of the Wärtsilä marine engine used for model identification and validation.

Displacement / Nominal speed	8.80 L / 1000 rpm
Stroke/Bore	1.4
Air system	Two-stage turbocharged (in series)
High-reactivity fuel system	Common rail
Low-reactivity fuel system	Low-pressure; multi-point, upstream of the intake valve
Valve train	4 valves per cylinder, fully variable hydraulic valve train
Emission system	Horiba Mexa-One (NO_X, CO, THC, CO_2, O_2) AVL415S (FSN-Soot)
Indicative system	AVL Indicom, Cylinder pressure tranducer Kistler 6124A, 300 bar range, 30pC/bar sensitivity.
Engine control system	Speed Goat / CanApe Rapid control protyping platfrom
Test fuels	ISO 8217 compliant LFO / NG (MN = 80)

injected using the common-rail injector with short durations and early injection timings characteristic of RCCI. Data used for model validation included crank-angle-resolved pressure traces in the cylinder. These signals were recorded for 300 consecutive cycles, with 0.2°CA resolution, at each steady-state operating point. In-cylinder pressure was further postprocessed to obtain combustion indicators, like indicated mean effective pressure (IMEP) and the crank angle of X% mass burned (CAX). Low-frequency measurement included the consumption of individual fuels (Coriolis flow meter and gravimetric fuel balance for gaseous and liquid fuel respectively) and air, intake and exhaust pressure and temperatures. The measurement campaign also covered detailed thermal characterisation of the charge at intake and exhaust ports and component temperatures (piston top, liner, valves and cylinder head) at different operating conditions. These served as boundary conditions for the simulation models.

2.2. The UVATZ combustion model

The governing assumption of the approach is in the simplification of fluid dynamics in favour of utilising computation resources for chemical kinetics. Therefore, it is assumed that in-cylinder flow is axisymmetric, and the combustion chamber is apportioned into ring-shaped zones which all share a common pressure (P_{cyl}), based on a Lagrangian perspective. Each zone is modelled as a homogeneous reactor, with the zonal arrangement shown in Fig. 1. Zones 1–10 are annular cylinders, while 11 and 12 are disc-shaped. Zones 10, 11 and 12 correspond to the lumped boundary regions of liner, piston and cylinder head, respectively, and exchange heat with the environment. Thus, the bulk influence of thermal stratification is reflected within UVATZ. The previous study [23] showed that 12 zones enabled UVATZ to capture the RCCI heat release profile sufficiently well.

Each zone is governed by the well-known coupled set of ordinary differential equations (ODE) for mass, energy and chemical species balance [25], including the contribution from interzonal flows. The interzonal exchange of heat and mass is modelled on a quasi-physical basis, since momentum conservation is not solved [11]. Despite sharing a common pressure, each zone (z) is characterised by its own temperature and composition. Assuming ideal gas, the equation of state for each zone is Eq. (1), with P_{cyl} indicating the shared instantaneous cylinder pressure. The constraint imposed via Eq. (2) maintains consistency with cylinder volume (V_{cyl}). Equations (1) and (2) are applied as a whole on the reactor network. A consequence of Eq. (2) is in its manifestation as interzonal work exchange (by movement of the interzonal boundaries) indicated by black arrows in Fig. 1. The author's review work [11] provides further details on this.

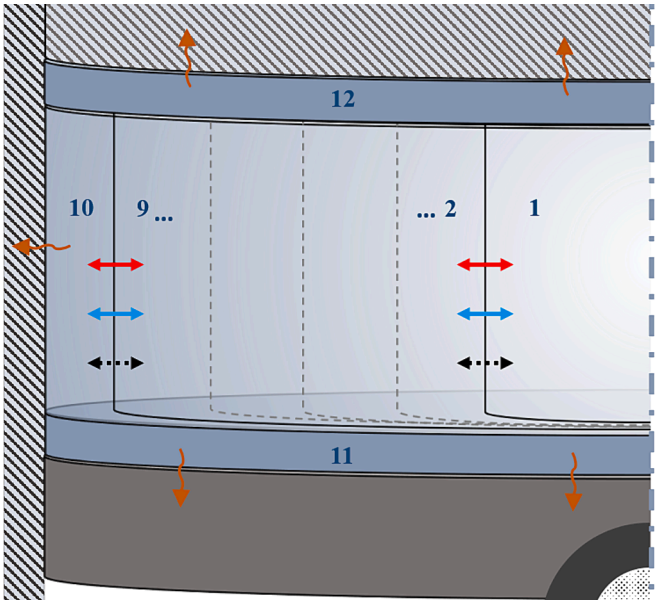

Fig. 1. Schematic of the zonal arrangement of UVATZ: red arrows indicate heat transfer; blue arrows indicate mass transfer; black indicate work transfer.

$$P_{cyl}V_z = m_z\frac{R_u}{\overline{W}_z}T_z \tag{1}$$

$$V_{cyl} = \sum V_z \tag{2}$$

The phenomenon of turbulent mixing on combustion is assumed to be diffusion-driven heat and species exchange between zones, depicted by the red and blue arrows respectively in Fig. 1. As indicated, each zone exchanges heat with all its immediate neighbours. However, for mass transfer with the boundary zones, annular zones 6–10 mix with the piston boundary zone, whereas annular zones 1–5 mix with the head boundary zone. Flux between zones z and $z+1$ is assumed to follow diffusion mechanism (Eqs. (3) and (4), with $\Delta T/\Delta w$ being the temperature gradient and $\rho\Delta Y_i/\Delta w$ being the concentration gradient of species i. Additionally, it is assumed that interzonal mass transfer applies to all species except for the HRF species. The basis for this assumption is associated with the approach of fuel injection modelling, explained in section 2.2.1. The coefficient Λ is thermal conductivity and $\mathfrak{D}$ is molecular diffusivity. The latter is obtained via the unity Lewis assumption. ${}^{M}\zeta_t$ and ${}^{H}\zeta_t$ are the mixing intensity factors for mass and heat transfer respectively, thus reflecting the influence of turbulence. This quantity is obtained from an in-cylinder turbulence model, discussed in section 2.2.2.

$$\dot{m}_{i,z\to z+1} = \begin{cases} M\zeta_t\left(\mathfrak{D}\rho\dfrac{\Delta Y_i}{\Delta w}\right)_{z\to z+1} & i \neq \text{HRF} \\ 0 & i = \text{HRF} \end{cases} \tag{3}$$

$$\dot{Q}_{z\to z+1} = {}^{H}\zeta_t\left(\Lambda\frac{\Delta T}{\Delta w}\right)_{z\to z+1} \tag{4}$$

Finally, heat loss across combustion chamber boundaries is modelled via the correlation by Chang et al. [26] based on the local properties of zones 10 – 12. The surface temperatures of liner, piston and head are imposed as fixed boundary conditions obtained from measurement data. For a complete account of the model equations, interested readers are referred to the previous work by the authors [23]

2.2.1. High-reactivity fuel stratification

The decoupled nature of injection and combustion phasing in RCCI [27] allows the HRF spray phenomenon to be modelled in a simplified manner. Thus, details of the spray development process may be disregarded with focus shifted directly to the ensuing bulk in-cylinder stratification which triggers combustion. With the spray emanating from a multi-hole injector, it is assumed that the bulk fuel inhomogeneity nearing start of combustion (SOC) is in the radial direction of the cylinder. As such, the HRF in UVATZ is directly injected as vapour into the annular zones (1–10) according to a predetermined profile at the moment of SOI. The enthalpy of evaporation is simply accounted for as proportional to the injected fuel mass in each zone. It is worth mentioning that only single injection events will be dealt with throughout this work.

It is because of this modelling approach to fuel injection, that interzonal mass transfer for HRF is excluded (Eq (3). The HRF distribution profile in previous works was considered as an operating case-dependent tuning parameter, typically due to absence of CFD data. Mikulski et al. [13] parameterised the distribution as a linear profile with richest zone located at liner, while Egüz et al. [10] used a bell-shaped profile, with the richest zone in the middle of the zonal configuration. Although these distribution profiles differ, they are conjectures

drawn from CFD [10] and optical studies [28], considering injector/piston-cylinder geometry and injection timing trends. In the recent work of the authors [23], a linear profile was used, then calibrated to fit simulation results with measurements.

This is remedied in the present work by extracting the HRF distribution profile from CFD results. This ensures that the imposed HRF stratification is realistic, but makes the approach reliant on CFD data on a case-by-case basis. Bearing in mind with this study's goal of establishing a performance-oriented model, autonomy of UVATZ is improved by formulating an empirical HRF distribution function, derived from a design of CFD spray simulations. This maps the HRF distribution profile to the engine's operating parameters. This methodology will be further discussed in section 2.4.

2.2.2. Turbulence-based interzonal mixing

In order to capture the influence of in-cylinder fluid flows within the framework of MZM assumptions, the mixing intensity parameter applied onto the gradient based flows is adopted, ${}^{M}\zeta_t$ and ${}^{H}\zeta_t$ in Eqs. (3) and (4) respectively. With the assumption of ${}^{M}\zeta_t, {}^{H}\zeta_t > 0$, implies that direction of flux still follows a negative gradient, but enhanced over molecular diffusion rate. Such an approach, whereby ${}^{M}\zeta_t = {}^{H}\zeta_t = \zeta_t$ set to a fixed (tuneable) value, has been proven to work well as in the case of HCCI [29], PCCI [30] and RCCI [13].

Building upon this approach, ${}^{M}\zeta_t$ and ${}^{H}\zeta_t$ in the present work are derived from a turbulence sub-model, in order to improve autonomy and the connection to fluid-flow physics. To this end, two approaches are investigated. The first is a popularly used empirical relation by Yang and Martin [19] which predicts variation of turbulent viscosity, based on in-cylinder condition and distance from wall. This simpler approach has been successfully used in many multizone modelling studies [18,31,32]. The model is applied over the closed part of the four-stroke cycle, and it is worth noting that it has only one calibration parameter. Further details on the implementation can be found in a prior work by the authors [23].

The second approach is a 0D turbulence model by Bozza et al. [33]. This is similar to the version implemented in the commercial tool, GT-Power. This belongs to the so-called *K-k* model family [34,35], which describes the energy cascade mechanism from macroscale kinetic energy (K) to turbulent kinetic energy (k). [33] includes explicit characterisation of the structured flow field of tumble motion. Therefore, the present implementation is governed by three ODEs: mean flow kinetic energy; turbulent kinetic energy; and tumble momentum, as illustrated graphically in Fig. 2. Turbulence dissipation is not directly modelled but derived based on user-imposed evolution of integral length scale. Since it is physics-based, this model is more sophisticated than the previous one. Importantly, it is capable of reflecting influence of boost pressure change, valve timing [34] and in cylinder geometry such as compression ratio and bore/stroke ratio [33]. The model has six tuning constants and CFD simulations provide the most comprehensive set of reference data for calibration. The methodology of this is explained in section 2.4. Interested readers are directed to the source [33] of the work for further details of this turbulence model.

In order to obtain the interzonal mixing intensity of mass (${}^{M}\zeta_t$) and heat (${}^{H}\zeta_t$) transfer from the turbulence model, an association is made with turbulent viscosity. By using turbulent Schmidt (Sc_t) and Prandtl (Pr_t) numbers a relationship is formed with ${}^{M}\zeta_t$ and heat ${}^{H}\zeta_t$, respectively, as shown in Eqs. (5) and (6). The basis for this relationship is derived from the assumption that the effective values of heat diffusivity and thermal conductivity are the sum of the molecular and turbulent components, Eqs. (7) and (8),respectively. For simulations, Sc_t and Pr_t are assumed unity.

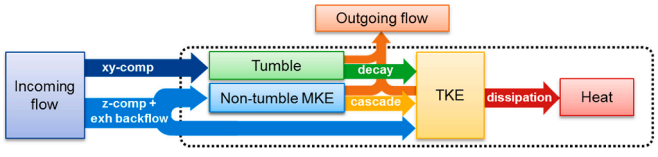

Fig. 2. Illustration of the approach for modelling turbulence by the K-k turbulence model from Kim et al. [36]: , Energies, published by MDPI, 2019. reproduced with permission from Kim et al. [36]

$$ {}^{M}\zeta_t = \frac{\mathfrak{D}_e}{\mathfrak{D}} = 1 + \frac{1}{\mathfrak{D}} \cdot \frac{\vartheta_t}{Sc_t} \tag{5} $$

$$ {}^{H}\zeta_t = \frac{\Lambda_e}{\Lambda} = 1 + \frac{1}{\Lambda} \cdot \frac{c_P \rho \vartheta_t}{Pr_t} \tag{6} $$

$$ \mathfrak{D}_e = \mathfrak{D} + \mathfrak{D}_t \tag{7} $$

$$ \Lambda_e = \Lambda + \Lambda_t \tag{8} $$

2.2.3. Solution algorithm and model initialisation

Chemistry is represented by the scheme of Yao et al. [37], where the HRF surrogate is $nC_{12}H_{26}$ and that for LRF is via a mixture of CH_4 and C_2H_6. A skeletal mechanism from Sun and Reitz [38] is supplemented for NO_x chemistry. The entire mechanism consists of 58 species and 281 reactions. Modelling of HRF stratification (section 2.2.1) requires the zone-wise fuel distribution to be prescribed as an input. These details are given in section 2.4.

With the UVATZ simulation running only over the closed cycle, model initialisation is via thermodynamic state at IVC, including the amount and composition of residual burnt gas. Good estimates of these quantities are necessary, concerning especially T_{IVC} and m_{iEGR}, since they exert significant effect on the accuracy of results [16,17]. This necessity also extends to the K-k turbulence model, which requires macro-scale kinetic energy, turbulent kinetic and tumble angular momentum to be correctly prescribed. Accordingly, the multizone framework is supplemented by a 0D gas exchange model, which assumes isentropic flow through valves. Boundary conditions needed by this approach are the compressor outlet and turbine inlet thermodynamic state, the data of which are obtained from measurements (section 2.3). Simulations are run as cycle-to-cycle connected, thus requiring 4 – 7 cycles for converged results. The convergence criterion is based on cycle-to-cycle variations in indicated mean effective pressure (IMEP), set as less than 1 %.

The modelling framework is implemented in C++ and deeply assimilated with the thermochemical libraries of Cantera [39]. Solution of the stiff system is obtained by employing the robust CVODES solver [40], with a typical simulation duration of about 3.5 min per cycle.

2.3. The CFD model

CFD simulations are used to obtain phenomenological insight into the processes of HRF spray and bulk in-cylinder turbulence, assisting development of UVATZ. Non-reactive simulations are sufficient. Fig. 3 shows the computational domain, which includes the cylinder, intake runner starting downstream of gas injector, exhaust runner and corresponding valves. The complete 3D representation of the domain is considered, thus accounting for the asymmetric nature of the flow field and including both open and closed part of the engine cycle.

The simulations are carried out in Converge Studio, using an unstructured type of background mesh with 10 mm resolution. A fixed embedding approach is incorporated in regions of the domain requiring finer resolution. Cell sizes are 1.25 mm for injection spray paths; 0.675 mm for intake port; and 0.3125 mm for exhaust port. Additionally, sub-grid scale-based adaptive mesh refinement is enabled, and the maximum cell limit is set to 500000.

In parcel modelling for fuel spray, the number of parcels is calculated based on the local cell size. The basic parcel cut-off specifications are set to 0.001 for the mass ratio of parcels and 1e-20 for their radius. The

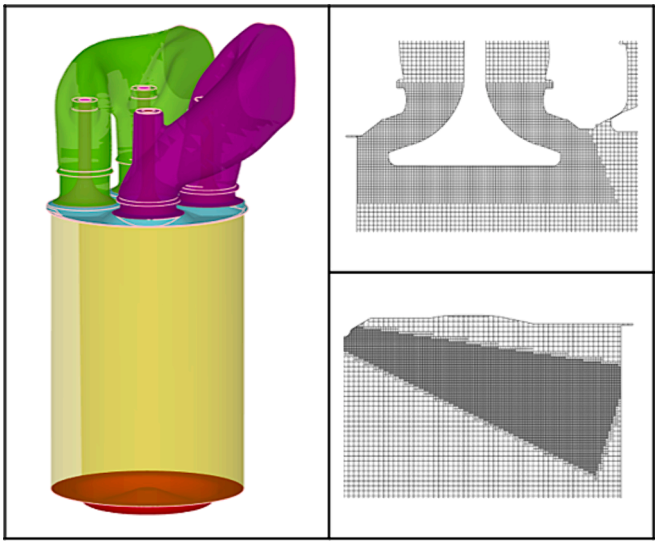

Fig. 3. Computational domain for CFD simulations, with piston positioned at BDC, including illustrations of the mesh in regions of the valve and spray path.

Rayleigh-Taylor (RT) model incorporating a chi-squared distribution is used to model liquid parcel atomisation and concentrated spray break-up. Additionally, child parcel creation is based on the Kelvin-Helmholtz (KH) model. Dynamic drop drag is employed for drag force calculation, using three dynamic drag variables with values of 0.083333, 10 and 8 respectively. The O'Rourke model accounts for turbulent dispersion. The Frosslig model is selected for evaporation of liquid parcels.

Turbulence is modelled using the Reynolds-averaged Navier-Stokes (RANS) approach of renormalisation group (RNG) k-ε model. To account for wall interactions, the law of the wall was chosen for the turbulent dissipation boundary condition, allowing a more accurate description of turbulent dissipation rates near the walls. Heat exchange from fluid to wall is represented by the O'Rourke and Amsden model, and the standard wall function was applied for near-wall treatment, providing robust and efficient predictions of flow characteristics near the boundaries. Additionally, the assumption of negligible absolute roughness and roughness constant further refines the law of the wall treatment, simplifying the modelling of wall effects.

The boundary conditions are obtained from a 1D air-path model (GT-Power), which is based on processed experimental burn rates. The data include the intake and exhaust manifold mean pressure, temperature, velocity magnitude and surface-averaged temperatures of cylinder head, piston, liner and intake and exhaust valve heads. The same surrogate fuels as presently used in UVATZ, are employed. This also applies to the physical properties such as surface tension, vapour pressure and viscosity.

This CFD model has been thoroughly calibrated for the scope of the present research in an earlier work by the authors. Complete calibration methodology and validation results on the same geometry are available in the publication by Kakoee et al. [41] and will not be discussed in detail here. For the sake of completeness, Fig. 4 shows results of the pressure trace and heat release profile. The model is calibrated to case B, while cases A and C serve for validation. The pressure curve is reproduced within and accuracy of 1.35 bar RMSE, with peak pressure around 1.2 % relative error. From the heat release profile, CA50 is on average within 1°CA and net heat released under 1.4 % error. Since the CFD combusting results are produced for close-cycle operation, the minor deviations in results and be attributed to inaccuracies in the initial conditions, especially temperature and mixture strength.

2.4. Scope of research and methodology for model calibration

Three steady-state operating points from the experimental platform (section 2.1) are selected as baseline conditions. They represent RCCI operation across the engine's load range, as shown in Table 2. The data is presented with respect to a reference 25 % load conventional dual-fuel calibration on the engine (Table 1), shown as *ref*. λ is the total air–fuel equivalence ratio, including both fuels. SOI refers to the start of injection for HRF (LFO in particular). The blend rate quantifies the amount of natural gas in the dual-fuel mixture defined on an energy basis. Temperature (T) and Pressure (P) with subscript "iman" denote the intake manifold thermodynamic state, measured at a point just downstream of the turbocharger compressor. The engine is operated under fixed speed mode of 1000 rpm, representative of variable pitch propeller propulsion or gen-set application.

Table 2 also presents the strategy for calibrating and validating the modelling framework. Validation is exclusively based on the experimental data mainly employing the pressure curve and its derived quantities, i.e., apparent heat release and performance parameters. Worth noting that the apparent heat release methodology is kept unchanged when applied to either simulations or measurement data. However, model calibration is based on a combination of data from experiments and CFD simulations, the latter used for sub-models for in-cylinder turbulence and predictive HRF spray stratification.

The scope of research encompasses benchmarking the performance of the baseline UVATZ model, first. This includes the tried and tested [18,23] approach of Yang and Martin (section 2.2.2) to model interzonal mixing. The simpler approach for HRF stratification is chosen, as the tuneable linear profile (section 2.2.1). To this end, Eq. (9) defines the profile across the annular zones, starting from 10th zone (next to the liner), with the slope (ζ_{∇}) and intercept ($^{HRF}\lambda_{10}$) as tuning parameters. An automated tuning procedure is used to fit the two tuning parameters

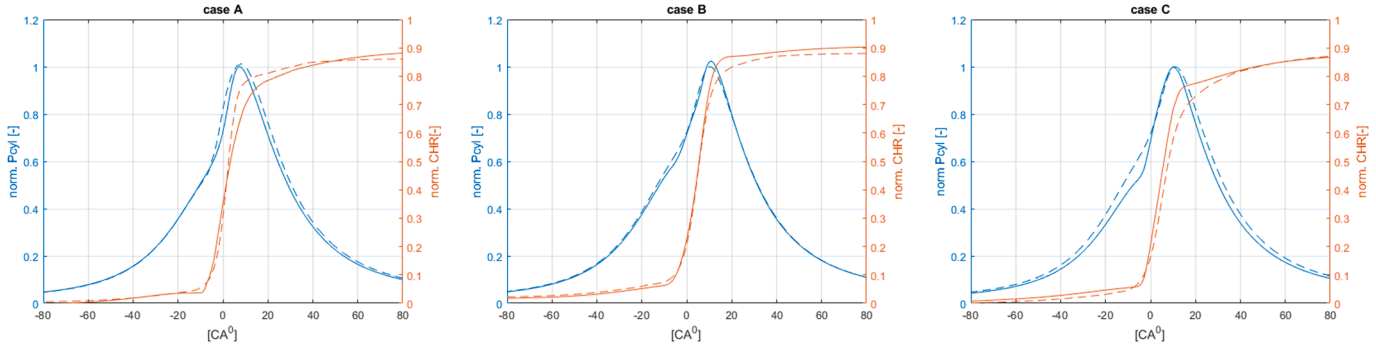

Fig. 4. From left, validation results of the CFD model (solid line) against measurement data (dashed line) for cases A to C (with permission from the authors). Pressure trace is normalised to peak measured value and cumulative heat release (CHR) is normalised to total fuel energy.
reproduced from Kakoee et al. [41]

Table 2
Experimental operating points for model calibration and validation.

Case	RCCI operating conditions							Modelling framework calibration and validation				
	Load [%]	λ [−]	BR [pp]	SOI [°CA bTDC]	T_{iman} [K]	P_{iman} [bar]	IVC [°CA bTDC]	CFD	UVATZ baseline	K-k sub-model	HRF strat. sub-model	UVATZ improved
A	21	ref	ref	ref	ref	ref	ref	Calibration (exp)	Calibration (exp)	Calibration (CFD)	–	Validation
		+0.54	−6.85	+36	+35.4	+0.31	+0.24					
B	50	ref	ref	ref	ref	ref	ref	Valdation	Calibration (exp)	Calibration (CFD)	–	Validation
		+0.63	+0.55	+31	+14.8	+1.92	−17.5					
C	75	ref	ref	ref	ref	ref	ref	Calibration (exp)	Calibration (exp)	Calibration (CFD)	Calibration (CFD-DoE)	Calibration (CFD)
		+0.51		+28	+7.1	+3.29	−34.5					

based on minimising the residual error to the experimental pressure signal. This benchmarking is performed for all three operating points as indicated in Table 2.

$$^{HRF}\lambda_z = {}^{HRF}\lambda_{10} + \zeta_\nabla \cdot (10 - z) \quad z = 1 \cdots 9 \tag{9}$$

In order to utilize CFD simulations, the model is first validated under reactive conditions for case B, as discussed in (section 2.3) using the boundary conditions in Table 2. The data on fluid flow and turbulence required for calibration of the *K-k* turbulence model, are then obtained via non-reactive, full-cycle (4-stroke) simulations carried out by imposing the same boundary conditions listed for cases A to C. The CFD results are then postprocessed to obtain mass-averaged values of turbulent kinetic energy (TKE) and turbulent dissipation rate (TDR) as the main quantities of interest. The integral length scale and turbulent viscosity are derived from this, using Eq. (10) and (11) respectively. Additionally, the tumble momentum is straightforwardly obtained from the elementary components of angular momentum (Eq. (12) following [33].

$$l_I = 0.084^{\frac{3}{4}} k^{\frac{3}{2}} \Big/ \varepsilon \tag{10}$$

$$\vartheta_t = 0.084 \frac{k^2}{\varepsilon} \tag{11}$$

$$L_T = \sqrt{L_x^2 + L_y^2} \tag{12}$$

Turning to HRF stratification derived from CFD data, the previously mentioned simulations are used, which have fuel spray modelling included. From the results, the radial profile of HRF concentration is obtained by averaging along the azimuth direction (θ) over the whole cylinder volume according to Eq. (13). The field data of local fuel–air equivalence ratio $\phi_{HRF}(x,y,z)$ is used for this purpose, as opposed to using λ_{HRF} to avoid singularity. Here x and y are parameterised in terms of radius (r) and θ, as $x = r\cos(\theta)$ and $y = r\sin(\theta)$. h is the height from piston crown to firing deck. $\widehat{\phi}_{HRF}$ profile is computed at a particular crank angle, the choice of which will be further described in (section 3.3). Once calibrated, this sampling angle is fixed for all load cases.

$$\widehat{\phi}_{HRF} = \frac{1}{h}\int_0^h \left[\left(\int_0^{2\pi} \phi_{HRF} \sqrt{\left(\frac{dx}{d\theta}\right)^2 + \left(\frac{dy}{d\theta}\right)^2}\, d\theta \right) \Big/ \left(\int_0^{2\pi} \sqrt{\left(\frac{dx}{d\theta}\right)^2 + \left(\frac{dy}{d\theta}\right)^2}\, d\theta \right) \right] dz \tag{13}$$

Furthermore, to alleviate the work of determining $\widehat{\phi}_{HRF}$ on a case-by-case basis, a simple predictive approach is conceived, which maps the appropriate stratification profile to a given operating condition. To this end, a response surface model (RSM) is chosen. The selected predictors are the operating parameters of SOI, charge density at IVC (ρ_{IVC}) and mass of HRF, all straightforwardly derived from ECU signals. Studies [42,43] show that the first two parameters largely influence the level of in-cylinder fuel stratification under RCCI conditions. ρ_{IVC} enables to capture influences of both T_{IVC} and boost pressure. Furthermore, the engine operates at a fixed speed and constant rail pressure, so these two parameters are excluded. Mass of diesel is necessary to obtain information on the amount of HRF injected per cycle. The RSM is then setup by running additional CFD simulations based on a two-level full factorial design as shown in Fig. 5. Case C is chosen as the baseline condition, at the corner of the design, indicated by the red circle. The motivation for this choice, as opposed to a design with a conventional centrally located baseline condition, is a matter of feasibility. This may be explained by taking the example of case B, wherein the setpoint values for *SOI* and m_{diesel} lie far away from their respective midpoint values between A and C. On the other hand, a design with case A as baseline, located at the bottom corner, is equally feasible. For the present design, the limits of the operating parameters are defined with reference to setpoint value as *SOI*: +10°CA bTDC, m_{diesel}: –15 mg and ρ_{IVC}: –2.4 kg/m^3.

Since case C is selected to setup the RSM for HRF stratification, the approach is validated with UVATZ under combusting conditions against cases A and B (last column of Table 2). The simulation in this section

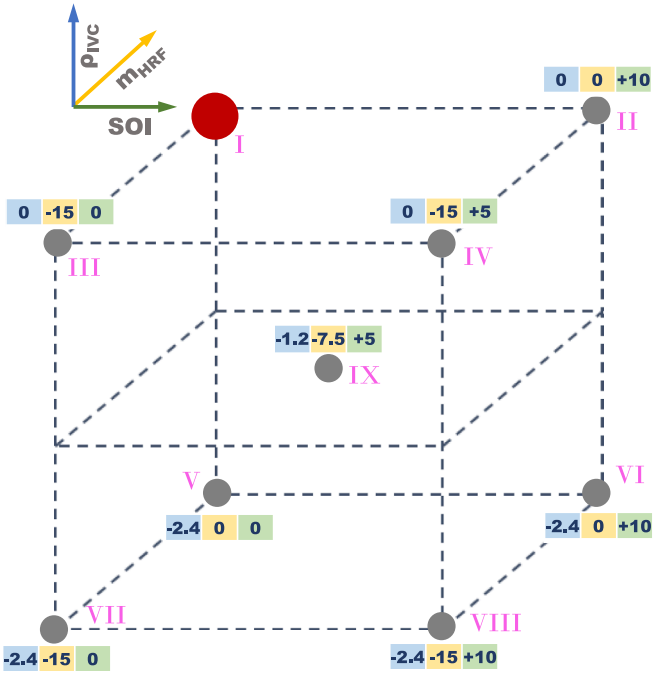

Fig. 5. Simulation cases for creating the RSM for HRF stratification profiles, coded with respect to baseline conditions of case C (red circle).

include the contribution of the *K-k* sub-model in combustion predictions. Further, a feasibility verification of the RSM is performed over a broader domain via sweeps of SOI, *BR* and λ, and the trends in predictions corroborated by similar experimental investigations from literature. This approach is followed to retain scientific rigour inspite of the limited experimental data. Emission specific model calibration and validation for NO_X and UHC predictions are assessed against all three operating points.

3. Results

3.1. Baseline model validation

Simulations of the baseline UVATZ framework are assessed first to benchmark of baseline model's performance. The three RCCI operating conditions from Table 2 are used. The baseline model employs the interzonal mixing approach of Yang and Martin (section 2.2.2). Modelling of HRF stratification is the non-predictive approach of a directly imposed profile according to Eq. (9), where the tuning parameters, ${}^{HRF}\lambda_{10}$ and ζ_{∇}, are determined for each operating case based on an automated fitting procedure (section 2.4). In addition, the IVC conditions are obtained by cycle-to-cycle connected gas exchange via a simple plenum model as explained in section 2.2.3.

For the sake of discussion, detailed plots of pressure, heat release and gas exchange are provided for the high-load operating point, case C. The final part of the section assesses model performance over all operating points, based on synthetic performance indicators. Raw pressure data from the multizone model exhibit jagged features as shown in Fig. 6a, which is then smoothened by employing a simple moving average filter. The net cumulative heat release (CHR) is computed from the raw pressure trace, shown in Fig. 6b.

For tuning the model to case C, a value of 3.8 is selected for ${}^{HRF}\lambda_{10}$, and ζ_{∇} is determined based on seeding the remaining fuel among zones 1 to 9 according to Eq. (9). Thus, the piston and head boundary zones (11 and 12) are not seeded with HRF. Fig. 7a shows the resulting stratification profile. It is important to note that an upper limit of 100 is set on ${}^{HRF}\lambda_{z}$, which prevents the inner zones from becoming too lean to ignite. This value is selected based on experience from our previous studies on multizone modelling for RCCI engines [2]. Also shown in the plot is the zone volume distribution, which is fixed for all operating points. This has been calibrated based on fitting the simulated CHR to measurements, with details elaborated in [23]. It is worth mentioning that piston and head boundary zones are each initialised to 2.5 % of IVC cylinder volume.

Fig. 6a shows that the pressure signal is reproduced well by UVATZ. The RMS error to the measured signal is < 2.7 bar, with error in P_{max} about 0.7 % and position of P_{max} overestimated by 3°CA. Further inference can be obtained from the apparent heat release analysis in Fig. 6b. Heat release is predicted well during the initial phase until about CA10, where the absolute error is about 0.7°CA. However, prediction of CA50 is delayed, with the error being 2.5°CA. Consequently, combustion which initiates in the liner zone progresses relatively slowly until 35 %

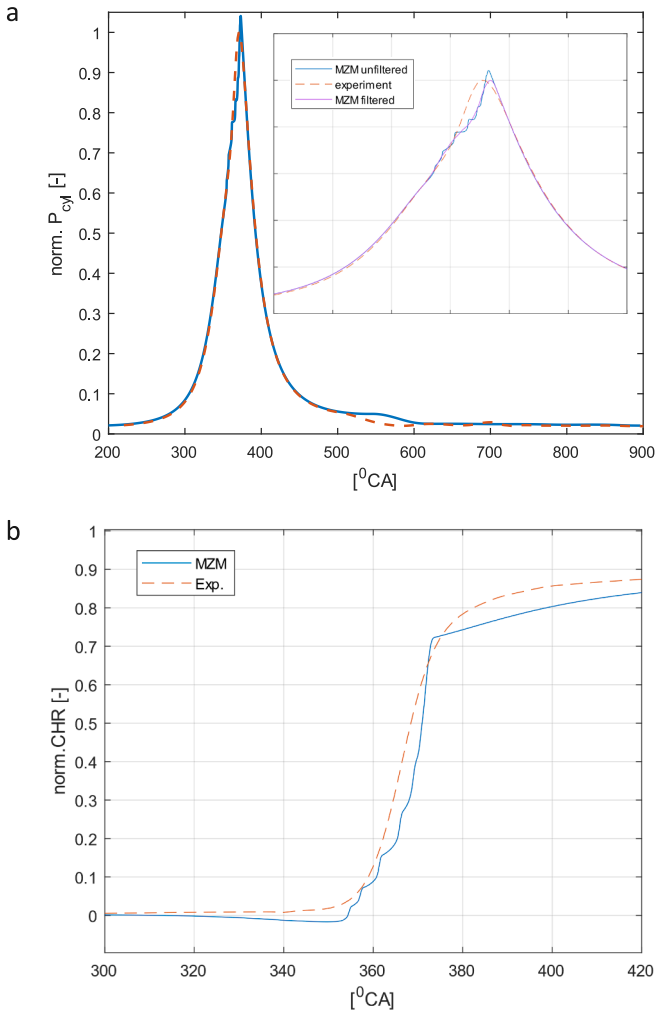

Fig. 6. Comparing simulated and measured (a) in-cylinder pressure normalised to experimental P_{max} and (b) net cumulative heat release CHR normalised to total fuel energy for case C.

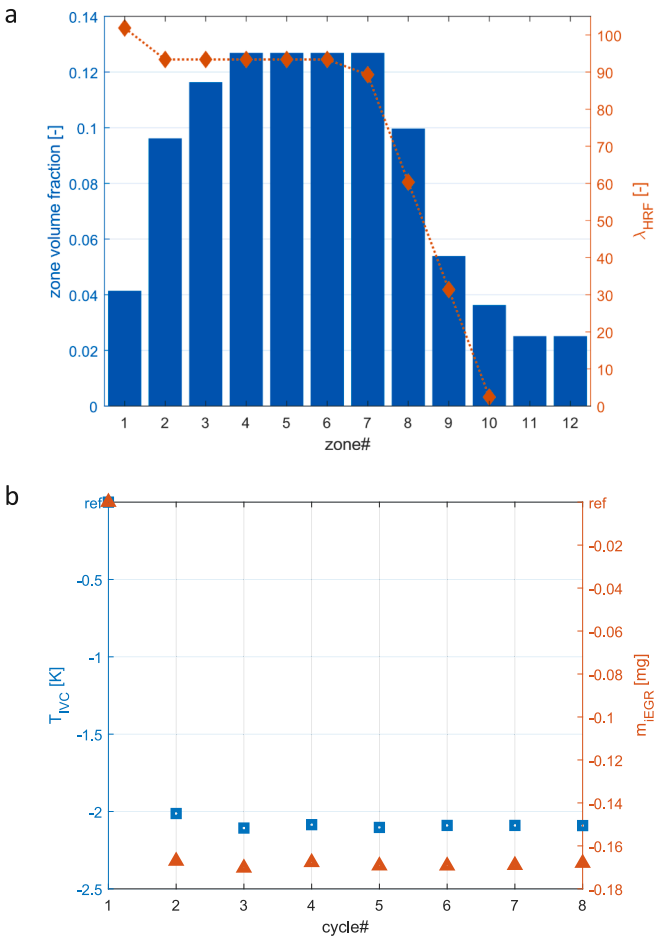

Fig. 7. (a) zone size (volume fraction) and zone HRF stratification profile as λ_{HRF} (b) IVC temperature and mass of internal EGR with 'ref' indicating conditions of case C from experimental dataset.

heat release mark which corresponds to ignition of zone 6. After this point, combustion progresses rapidly, indicated by the steep slope of CHR. This persists until the 75% of heat release mark, corresponding to 15°CA aTDC, when most zones have combusted. The final retarded phase, indicated by the sharp change in slope, encompasses ignition of 12th zone (head) followed by cooling of the burnt gases due to heat loss.

Despite good predictions of the salient points such as CA50, predictions of CHR and the pressure trace need improvement. Increasing the number of zones would address this, but alternative solutions with an improved interzonal mixing model and fine-tuned zone sizing are more appealing, because they do not impact simulation speed. The interzonal mixing intensity by the Yang and Martin approach in the current simulation is nearly constant with time (explained in section 3.2) and its calibration is based on balancing the delay in heat release during the initial phase with the rapid propagation during the latter phase. The net heat released observed at the end of combustion is within 3.7 % error to experimental data, resulting from a proportional error in the predicted residual unburnt fuel.

The above results are obtained by virtue of appropriate IVC conditions via the gas exchange process. Fig. 7b shows the variation of IVC temperature and mass of residual burnt gas (iEGR) from their initially estimated value at first cycle. It can be observed that 4 – 6 cycles are sufficient for converged solution. Mass of iEGR is determined by the difference between the in-cylinder mass at IVC and the integrated mass flow across intake valve. While the trapped mass and cylinder thermodynamic state are updated with each cycle, temperature and residual burnt gas are shown here, as these parameters have a large bearing on RCCI combustion.

Fig. 8 summarises the model's overall performance under all operating conditions. All performance indicators are within the stipulated 5 % error limit. Heat release is characterised by the quantities CA10, CA50 and neat heat released (NHR). Although the error in CA10, CA50 and position of peak pressure (Pmax.pos.) is less than 1 % (absolute error $<$ 3°CA), it is systematically overpredicted. This indicates an underlying underprediction of mixture reactivity and is primarily associated to chemical kinetics scheme. P_{max} and net indicated mean effective pressure (IMEP720) characterise the pressure curve. Volumetric efficiency (Vol.eff.) and scavenging efficiency (Sca.eff.) characterise the gas exchange process, specifically the intake mass flow and total trapped mass. It can be observed that the error in NHR, IMEP720 and Vol.eff. are relatively large, and is attributed to the imposed boundary conditions, i.e., P and T of intake and exhaust manifold. This can be alleviated by directly coupling to a detailed 1-D air-path model.

3.2. Predictive turbulence model validation

Validation of the turbulence model is assessed mainly based on predictions of turbulent viscosity (TKV), since it is the quantity of interest, associating turbulence to interzonal heat and mass flows (section 2.2.2). To this end, cold-flow CFD simulations over the full cycle are employed. Performance of the Yang and Martin based approach is discussed first, shown in Fig. 9. It can be observed that the model predicts a near constant value over the whole duration, markedly different from CFD results. The CFD derived TKV shows little variation across the operating points, demonstrating minor sensitivity to load change. However, the initial decay in TKV until TDC is not captured by the approach based on Yang and Martin. This behaviour of the model is expected as the correlation predicts mainly the 1D variation of TKV across boundary layer. Nevertheless, by appropriately calibrating the model during the main phase of combustion (350-400°CA), turbulent viscosity can be approximated as has been shown to work sufficiently well in previous studies [18,23,31,32].

In pursuit of the research goals, the *K-k* model is implemented in an attempt to improve fidelity of fluid flow physics, and consequently autonomy and predictivity. In line with observations by De Bellis et al. [34], the integral length scale does not vary much with operating conditions. This enables it to be modelled as a simple piecewise function composed of sinusoids and lines, and the fit against CFD results is shown in Fig. 10. Based on this, the 0D turbulence model is then calibrated to fit accordingly to all three experimental cases under cold flow condition, as shown in Table 3. The *K-k split factor* determines the fraction of inflow kinetic energy that directly enters the cylinder as turbulence, and its value is calibrated to 3 %. *Turbulence production multiplier* acts on the term for energy cascade mechanism from mean flow kinetic energy to turbulent kinetic energy. *Decay function offset* and *Decay function multiplier* are associated with the decay function which models the decay of mean flow kinetic energy and tumble momentum due to wall shear stress. The last two parameters are associated to modelling the characteristic scale of tumble vortex, following the formulation of [44]. For the background on the tuning constants in the context of the governing equations of the *K-k* model, the reader is directed to the source material [33].

Note that although the calibration constants are tailored to the Wärtsilä 20 engine geometry (Table 1), the model is expected to capture the trends in results when directly applied to a different engine geometry. For absolute level accuracy, however, retuning is strongly recommended. To this end, while CFD simulations are most convenient, calibration based on engine test dataset is also possible.

Results of the calibrated turbulence model are depicted in Fig. 11, assessed against CFD results of TKV, turbulent kinetic energy (TKE),

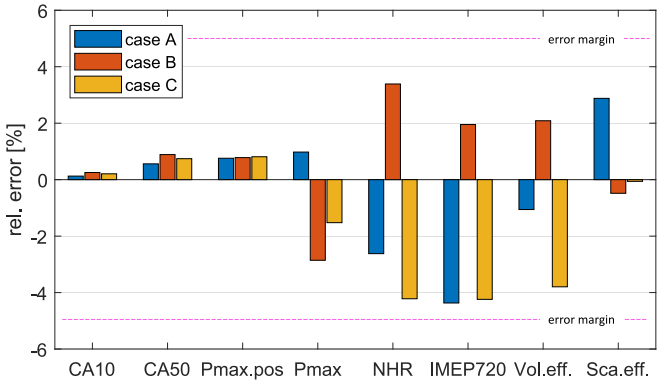

Fig. 8. Error in performance indicators prediction by UVATZ against measurements.

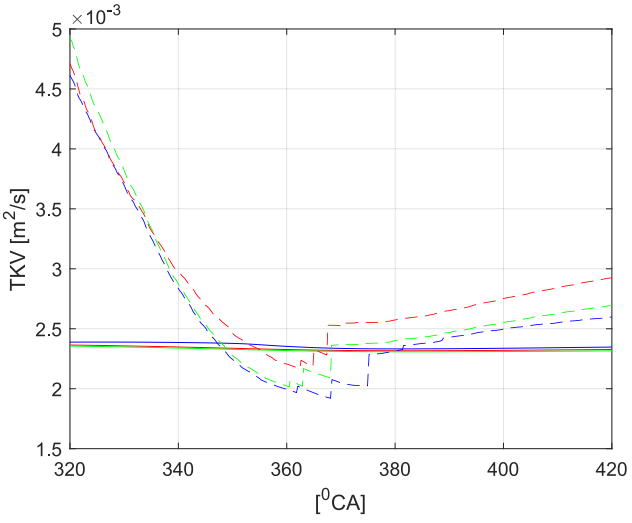

Fig. 9. Comparison of turbulent viscosity from CFD results (dashed lines) against the Yang and Martin approach (solid lines) for cases A (blue), B (red) and C (green).

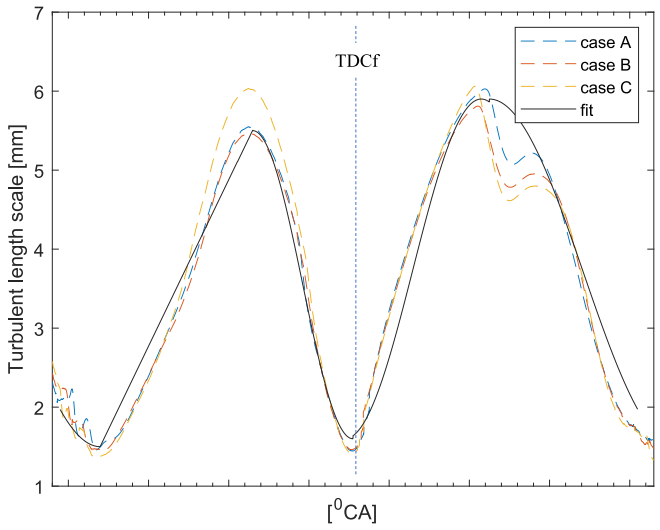

Fig. 10. Integral length scale reconstruction using CFD results.

Table 3
Calibrated tuning constants of K-k model to W20 RCCI engine.

K-k split factor	0.03
Turbulence production multiplier	1.13
Decay function offset	3.5
Decay function multiplier	0.7
Tumble radius offset	0.35
Tumble radius multiplier	1.5

turbulent dissipation rate (TDR) and tumble momentum, for all three cases. The plots show full cycle histories of turbulence quantities, with 360° being compression TDC. It is worth noting that converged results of turbulence model are obtained within 2–3 cycles of simulation, depending on how well the initial values are estimated. The calibration effort has been focused on the closed cycle, mainly between end of injection (EOI) and end of combustion i.e., 200-400°CA.

Phenomenologically, it can be observed from the plots that the turbulence level does not vary much with the operating points. Boost pressure predominantly differs between the cases, and its influence is apparent in the increasing peaks in tumble momentum. Looking at the phases when CA $< 200°$ and CA $> 500°$, which correspond to the intake and exhaust stroke respectively, the flow field is rather complex and includes the initial phase just after IVC and end of expansion stoke. The details are not expected to be captured in a 0D approach. A further explanation for the discrepancy can be seen in TDR: this was not directly modelled, but simplified via the imposed integral length scale. Nevertheless, the general trend in the turbulence quantities is well represented.

Plots of TKE show that turbulent speed-up close to TDC is predicted slightly early. Being connected to the collapse of tumble motion, the model proves inadequate in representing the details as seen from corresponding plots at the bottom. It has been recognised [44] that the flow complexities in predicting tumble motion, which often consists of multiple interacting vorticial structures, is challenging to model as an equivalent single macro vortex. However, with the duration of the compression stroke bearing importance, TKE is predicted trend-wise sufficiently well with a relative root mean square error near 10 %. This is an improvement over the previously simplistic approach. Importantly, the *K-k* approach does not increase the computation burden, with simulation still taking about 3.5 min per cycle.

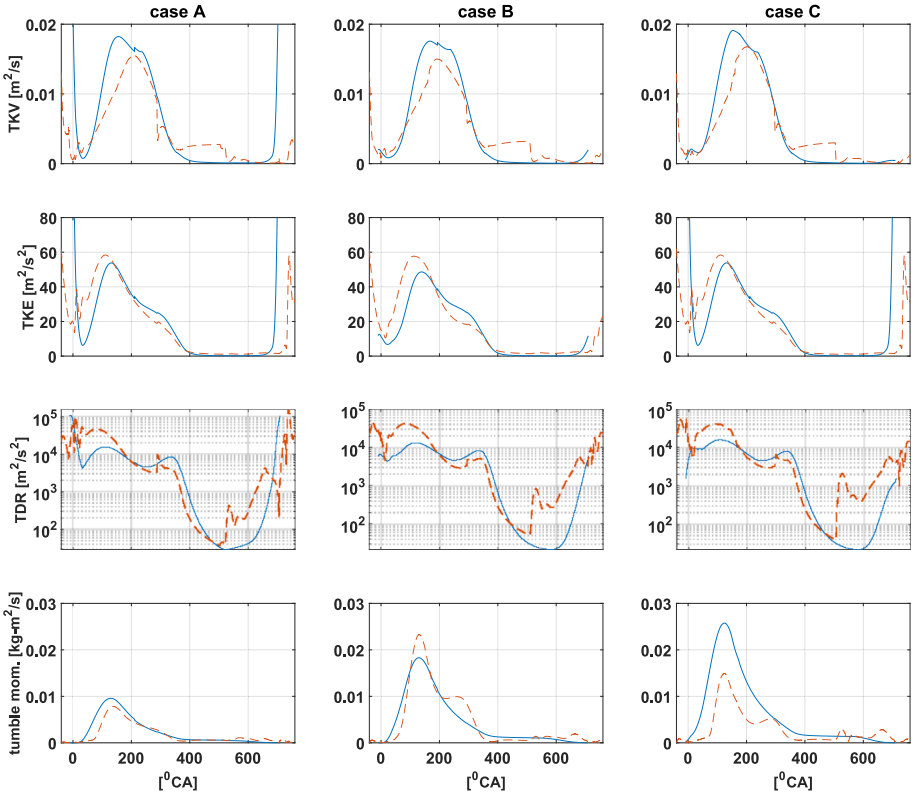

Fig. 11. From the top, predictions of turbulence kinematic viscosity (TKE); turbulent kinetic energy (TKE); turbulence dissipation rate (TDR); and tumble momentum from K-k model (solid blue line) against CFD results (red dashed line).

3.3. Calibration of CFD-derived HRF stratification

The stratification of HRF has thus far been modelled as a tuned linear (presumed) profile across the zones. This section explores the approach more grounded in fundamentals. To this end, the profile directly post-processed from CFD results is desired, and the process is illustrated in Fig. 12, which is based on case C. The first subplot shows the 3D data of local fuel–air equivalence ratio field obtained from the CFD simulation at 15°CA bTDC. This angle approximately corresponds to the instant when combustion initiates. It can be observed that high concentration areas of HRF are close to the liner, following the spray development process from the 9-hole injector. These data are postprocessed using the relation in Eq. (13). to obtain the averaged radial profile shown in Fig. 12b. The plot is made in $\log_{10}$ scale in terms of air–fuel equivalence ratio (λ_{HRF}), indicating an exponential decrease towards the cylinder axis. The datapoint at 0.1 m corresponds to the liner which is the richest with λ_{HRF} of 3.2. A straight-line approximation of the data is overlaid, and illustrates the correspondence with the previously held assumption (Eq. (9) regarding the shape of HRF stratification. It is worth noting that simulations for the other cases, A and B, revealed a similar trend.

In order to map the CFD-derived profile onto the zones of UVATZ, it first needs to be discretized, respecting the total mass of injected fuel. The basis is a routine similar to the previously utilised Eq. (9). Considering the exponential trend from Fig. 12b, modifications are made to the relation, as shown in Eq.14. The HRF concentration of the liner zone, ${}^{HRF}\lambda_{10}$, is taken directly from the CFD-derived profile, which for case C is 3.2. The other parameter, ζ_{∇}, is then adjusted until zones 3–9 are seeded with HRF, as seen in Fig. 12c. The assumption is justified since the innermost zones (1–2) are extremely lean. Therefore, the resulting value for ζ_{∇} of 0.27 is selected since it produced the best fit to experimental heat release profile. This routine is automated , so the CFD-derived stratification of any operating condition is mapped on to the zones. Importantly, the HRF stratification field from CFD results extracted at a sample angle of 15°CA bTDC produced the best combusting results, within the inspected range 30 – 10°CA bTDC. Thus, the sample angle considered fixed for all cases, works well with the mapping routine.

$$ {}^{HEF}\lambda_z = {}^{HRF}\lambda_{10} \cdot 10^{\zeta_{\nabla}(10-z)} \quad z = 1 \cdots 9 \tag{14}$$

Fig. 13 depicts combusting results for case C, based on this fuel distribution. It includes the filtered pressure trace and CHR profile post-processed from the model's raw pressure signal. These results are also a product of the *K-k* turbulence model, which has been considered in the calibration of the HRF stratification procedure. The pressure trace is predicted with an RMS error of 2.4 bar. The errors in P_{max} is 1.4 % with the position of P_{max} under 0.65 %, and IMEP720 approximately 0.6 % as shown in Fig. 13b. The predicted CA50 is obtained within an error of 1.5°CA. Importantly, the predicted heat release better matches the

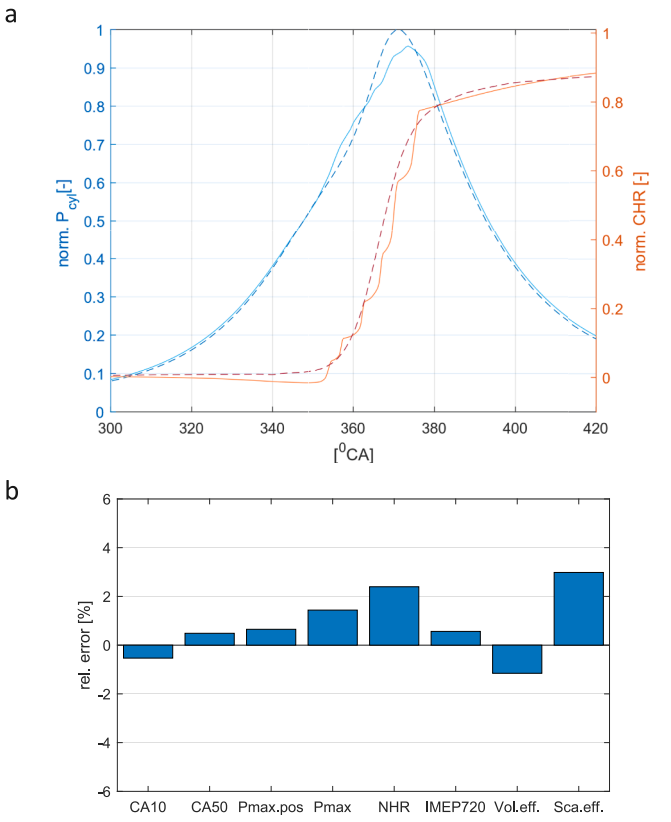

Fig. 13. Results for case C: (a) in-cylinder pressure trace from simulation and experiments, normalised to measured peak pressure; And cumulative heat release profile from simulation and experiments, normalised to total fuel energy; (b) error in predictions of engine performance indicators.

experimental trace and will be summarized in the section 4.2 in the context of overall model improvements.

Further insight can be obtained from the zone-wise heat release shown in Fig. 14a arranged in order of their respective ignition time (CA10). It can be observed that combustion initiates from the liner, zone 10, and proceeds inwards by virtue of the imposed HRF distribution (Fig. 12c). The spacing between each igniting zone is important – in determining the overall heat release shape. This has been used to recalibrate the zone sizing, shown in Fig. 14b. The highly reactive outer zones (9 and 10) ignite during the initial phase, elevating the overall cylinder temperature via interzonal heat transport. The radical pool consisting of, for instance H●, OH●, CH_3● and CH_3O●, are quickly transported towards the inner zones due to interzonal mass transfer. Therefore, the inner zones consisting mainly of CH_4-air charge,

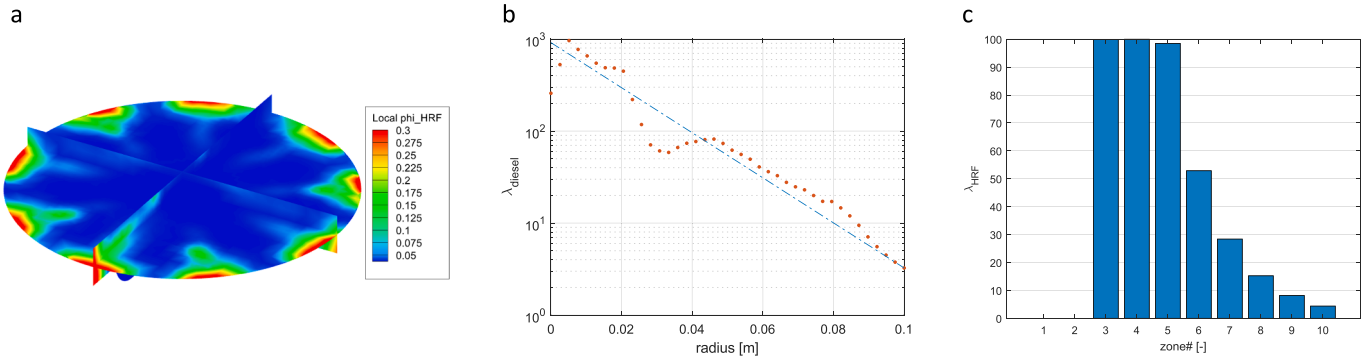

Fig. 12. (a) Local ϕ_{HRF} field from CFD simulation for case C at 15°CA bTDC; (b) postprocessed radial HRF stratification profile in terms of λ displayed in $\log_{10}$ scale: the raw data (red dots) is overlaid with a straight line approximation (blue line); (c) the corresponding HRF distribution mapped on to zones, shown in linear scale.

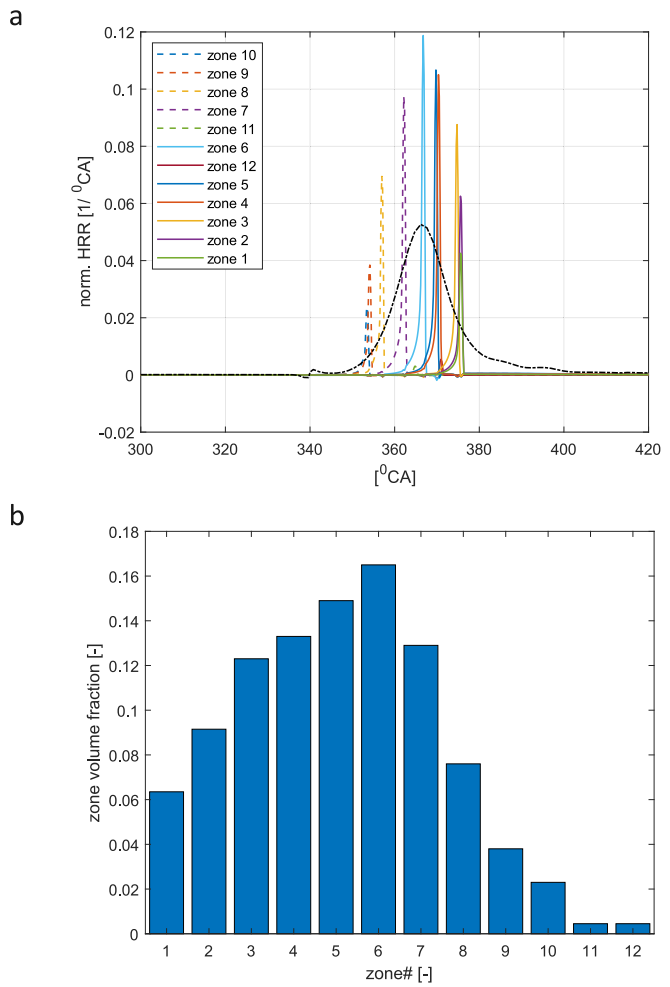

Fig. 14. (a) zone-wise heat release with the experimentally obtained heat release (black dashes), normalised to total fuel energy; (b) calibrated zone sizing (volume fraction).

successively increase in reactivity due to the elevating radical pool and temperature (>1000 K) required for the initiation reactions. Ignition of 6th zone approximately coincides with CA40, and has the largest amount of heat release rate. Combustion quickly progresses until ignition of 4th zone, where in-cylinder temperature reaches 1700 K and 70 % of the total charge is burnt. Then, HRR progressively slows down around 10°CA aTDC. There is a delay in ignition of the inner zone (1–3) due to greatly reduced interzonal mixing intensity.

In combination with the zone volume sizing, the progress of combustion in the zones is modulated by the interzonal mixing intensity, which is obtained from the turbulent viscosity (*K-k* sub-model). Fig. 11, shows that the magnitude between 200°CA and 360°CA (TDC) is larger than values between 360°CA and 400°CA. However, the previous results (section 3.1) based on the Yang and Martin approach, show that TKE remains nearly constant (Fig. 9) throughout the duration of combustion. And, it is worth mentioning the contribution of the zones 11 and 12 in combustion propagation to the inner zones. While their primary goal is for emissions modelling and wall heat loss, zones 11 and 12 additionally transfer heat from the early igniting outer zones (7 – 10) towards the inner zones, by virtue of interzonal heat transport. Despite this amount of heat being low, due to the small size and low temperatures of these boundary zones, it is typically sufficient to influence the inner zones to ignite, in addition to the mechanisms discussed above. This is another reason underpinning the design of the zonal configuration (section 2.1). Further details regarding sizing of zones 11 and 12 are discussed in Section 3.5. Ultimately, the improvement in predictions can be attributed to the *K-k* turbulence sub-model and recalibrated zone sizing.

3.4. Validation of semi-predictive HRF stratification sub-model

The aforementioned approach is augmented to obtain HRF stratification over a broad operating range. Instead of requiring CFD spray simulation on a case-by-case basis, an empirical approach is employed to determine HRF stratification. To this end, a response surface model (RSM) is selected and setup based on CFD simulations across a discrete set of points, according to the design explained in section 2.4. Thus, apart from case C, 8 additional CFD simulations are performed. SOI, charge density (ρ_{IVC}) and mass of diesel (m_{HRF}) are the chosen predictors. It is assumed that the stratification profile parameterised according to Eq. (14) varies linearly with the operating parameters. To further support this assumption, the limits of operating parameters are kept quite restricted, i.e., *SOI*: +10°CA bTDC, m_{diesel}: –15 mg and ρ_{IVC}: –2.4 kg/m^3, based on nominal conditions of case C.

To create the RSM for HRF stratification, following Eq. (14), a first order model with interaction terms (Eq. (15) is conceptualised solely for ${}^{HRF}\lambda_{10}$. The HRF distribution profile is then completed applying the previously discussed automated procedure, which computes ζ_∇ by seeding the remaining HRF from zones 3 to 9. The model for predicted ${}^{HRF}\lambda_{10}$ ($\widehat{{}^{HRF}\lambda_{10}}$) is shown in Eq. (15), where β_i are the model coefficients, the values of which are presented in the second column of Table 4. It is worth noting that the predictors are normalised based on the difference from their respective nominal to limit values. Also presented are statistical quantifiers that assess the RSM's fit to data, which include standard error of estimate (SE), t-statistic and p-value.

$$\widehat{{}^{HRF}\lambda_{10}} = \beta_0 + \beta_1 SOI + \beta_2 m_{HRF} + \beta_3 \rho_{IVC} + \beta_4 SOI{\cdot}m_{HRF} + \beta_5 SOI{\cdot}\rho_{IVC} + \beta_6 \rho_{IVC}{\cdot}m_{HRF} + \beta_7 SOI{\cdot}m_{HRF}{\cdot}\rho_{IVC} \quad (15)$$

Observing the magnitude of the coefficients (β_i) in conjunction with their p-values, reveal that all terms of the RSM contribute to the prediction $\widehat{{}^{HRF}\lambda_{10}}$. However, the relationship between β_4's magnitude and its SE implies a larger uncertainty in its estimate. Combined with the smallest t-stat, this reveals lower statistical significance of this term in the RSM. Still, with the associated p-value near 6 %, it is deemed sufficient for the purposes of this research. Finally, the overall analysis of variance of the RSM reveals a coefficient of determination (r^2) of nearly 1, wherein the F-statistic of 2.22x10^4 with the associated p-value of 0.0052 are achieved, revealing that the linear RSM reliably describes the calibration data.

With case C having been used to create the RSM, cases A and B are used for validating the approach based on combustion performance. As such, the zonal HRF distribution for the respective cases obtained from the empirical approach is shown in Fig. 15. λ_{HRF} in the 10th zone obtained from the RSM is 3.9 and 5.4 for cases A and B respectively. Furthermore, the plot shows that λ_{HRF} in all zones for case A is lower than that of case B, wherein the slope parameter (ζ_∇) is lower by 37 % for case A. This is because the BR for case A is nearly 6 pp lower than case B, owing to the quantity of diesel injected into the cylinder being

Table 4
Fitted coefficients of RSM (Eq. (15), including summary statistics on the regression.

Coefficient	Est. value	SE	t-stat	p-value
β_0	3.2501	0.0083	389.00	0.0016
β_1	1.1701	0.0118	98.506	0.0064
β_2	−1.6266	0.0118	−136.94	0.0046
β_3	−0.7991	0.0118	−67.284	0.0094
β_4	−0.1774	0.0168	−10.561	0.0601
β_5	−0.7128	0.0168	−42.432	0.0152
β_6	0.9711	0.0168	57.802	0.0110
β_7	0.3329	0.0237	14.0123	0.0453

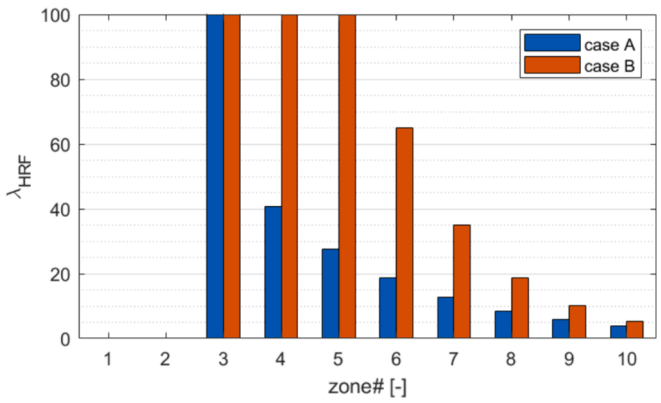

Fig. 15. HRF distribution among the zones for cases A and B, from the predictive HRF stratification procedure.

17 % larger, in combination with 47 % lower boost pressure for case A. These changes in the operating parameters are appropriately reflected in the zonal fuel distribution by the predictive HRF stratification procedure.

Based on inputs of fuel stratification (Fig. 15), combusting simulations are performed for cases A and B. The results are shown in Fig. 16, where a moving average filter applied over simulated pressure curve, compared against the measured data. The accuracy of the predicted pressure trace is with an RMS error of 1.01 bar for case A and 1.56 bar for case B. As such, error in P_{max} is within 4.7 % and 1.16 % for cases A and B respectively, and position of P_{max} under 0.5 %. From the heat release, relative error in CA10 for cases A and B is respectively 0.5 % and

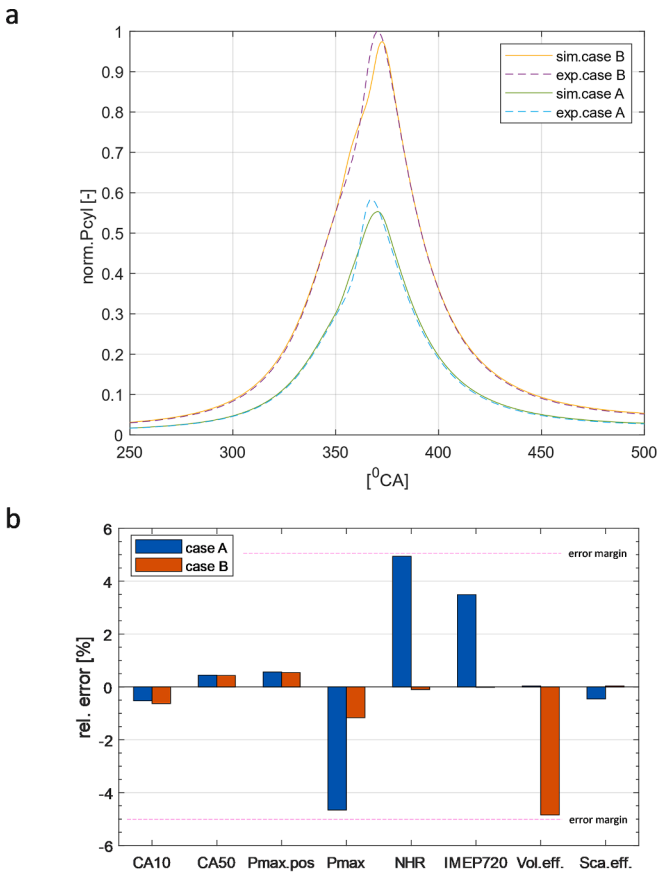

Fig. 16. (a) in-cylinder pressure trace from simulation and experiments, normalised to measured peak pressure of case B; (b) error in predictions of performance indicators for case A and B.

0.6 %; 0.4 % and 0.4 % in CA50; and 4.9 % and 0.1 % in NHR.

Despite the acceptable accuracy, it can be observed that error in IMEP720, NHR, volumetric efficiency is relatively large. This is more a consequence of inaccuracies in boundary conditions than due to the predictive HRF stratification procedure itself. The error for case A can be specifically attributed to inaccuracies in the amount of NG injected in the cylinder, since UVATZ does not have a lambda controller to adjust the cycle-to-cycle variations in the low reactive fuel. In case B, the error arises due to inaccuracies in the imposed intake and exhaust manifold boundary conditions. It is worth noting that small changes in these boundary conditions, typically < 3 %, manifests in large changes in the results for RCCI performance simulations. These shortcomings can be overcome by coupling with 1D modelling of the air and fuel paths, as will be discussed in section 5. Further insights on the performance of the predictive HRF stratification procedure are discussed in section 4.1 in the context of a parametric study.

3.5. Calibration for emissions prediction

The nature of LTC concepts means soot emission is negligible [45] and that of NO_X is quite small. However, in the case of NG-diesel fuelled RCCI, unburnt hydrocarbon emissions typically methane slip, is significant (section 1) calling for abatement measures such as combustion-specific calibration or a methane oxidation catalyst. Despite present IMO regulations (tier III [46]) mainly stipulating limits on SO_X and NO_X emissions, it is expected to also include UHC in the near future, as already being enforced by the European stage V inland waterways legislation and U.S. based EPA tier IV norm. Accordingly, emissions of UHC and NO_X are considered in the present study.

Accurate emissions prediction is an enormous challenge for predictive models such as UVATZ. Still, owing to the chemical-kinetics nature, the trends can be captured well enough. However, absolute level accuracy as reported in literature [11] varies largely, from 20 % to over 100 % error for UHC and NO_X emissions. For the present research however, a reasonable accuracy margin of 35 % is selected following the work of De Bellis et al. [20]. Worth noting that based on the employed chemical kinetics scheme (section 2.2.3) determination of NO_X emission is by thermal formation mechanism. It does not include the scheme for prompt NO_X formation.

Before calibration for emissions, it is worthwhile investigating the modelling characteristics of UVATZ that influence emissions prediction. Results of case B are chosen as a bases, from the simulations in section 3.4. Fig. 17 shows the zone-wise emission (zone mass fraction) of NO_X and UHC in addition to the zone temperatures. It can be observed from Fig. 17c that temperature of the outer zones (7 – 10) is the largest, since nearly 70 % (Fig. 15) of the HRF quantity is injected in them. Thus, owing to their large reactivity, combustion initiates in these zones. Zones 11 and 12 are coolest owing to their individual size (0.45 %(v/v) – refer Fig. 14b) relative to contact surface area, i.e., piston and head surfaces. As such, these are the smallest zones. The in-homogeneity in the thermal state of the zones enables prediction of emissions, as will be discussed.

Worth noting that in the present research, emissions tuning has been achieved mainly based on liner, piston and head zones (10, 11 and 12 respectively). In this context, it must be reported that, approaches such as a supplementary crevice zone [18] have been tested for the sole purpose of emissions predictions, but proved unsuccessful. The challenges included sizing of the zone, modelling of mass flow to and from crevice. Numerical stability was a particular issue, with tripled simulation time or frequent crashes. In contrast, the current approach did not bear any impact on simulation time, which remained around 3 min per cycle.

The plot of NO_X (Fig. 17a) shows that the outer zones (7 – 10) are the major contributors owing to the higher temperatures, which peak at almost 2000 K. In fact, NO_X concentration in zones 9 and 10 is over five times that of the inner zones. However, this is highly localised, since

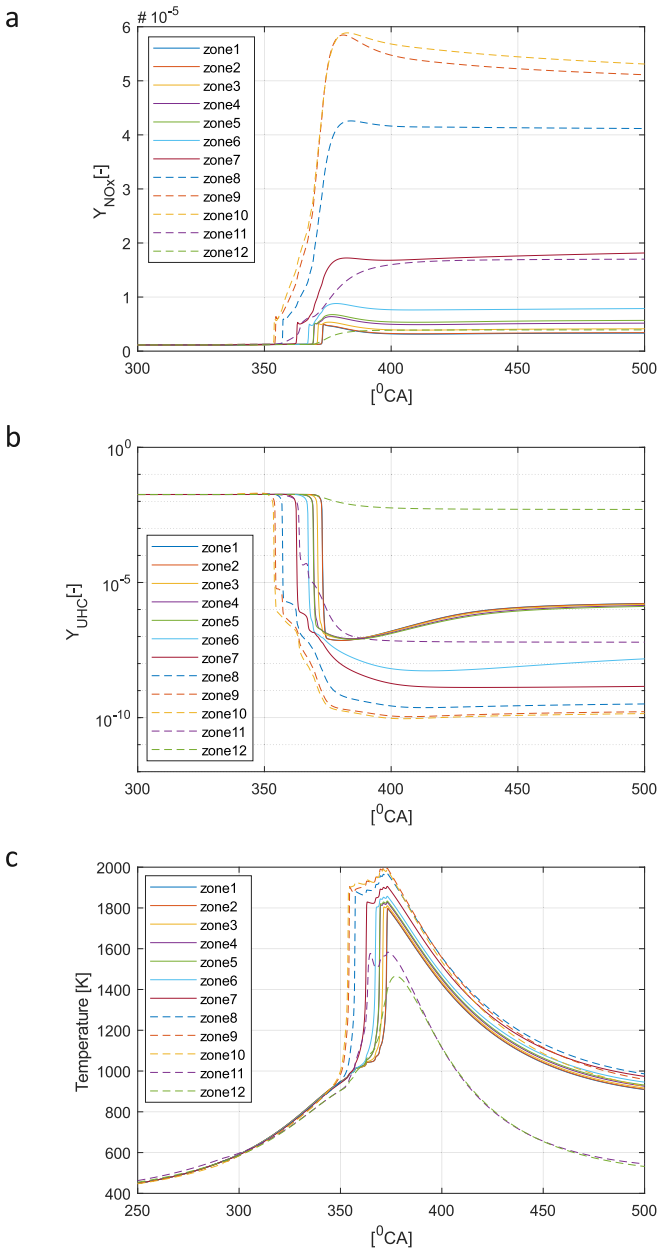

Fig. 17. Local (zone-wise) properties for case B: (a) NO_X mass fraction; (b) UHC mass fraction; (c) temperature.

zones 9 and 10 are only 2.3 % and 3.8 % respectively, of the in-cylinder volume. It can be observed that quite some NO_X concentration accumulates in the 11th zone despite its temperature being low (<1600 K). This is due to interzonal mass transfer from zones 7 – 10.

The composition of UHC include C1-C2 species, reflecting the combination of methane and ethane used to model NG. Ranked in terms of magnitude, UHC contains the fuel species itself CH_4 and C_2H_6 and formaldehyde (CH_2O), ethene (C_2H_4) and acetylene (C_2H_2) that are present in the mechanism. Fig. 17b shows that a large concentration of UHC is present in the head zone, owing to it being the coolest zone. Additionally, the inner zones (1–5) contribute to UHC emissions, but the concentrations are 5 orders of magnitude lower than that in the head zone. However, since zones 1–5 are much larger in volume than the head zone, their contribution to the total UHC emissions is much larger.

Additional insight is obtained via a sensitivity analysis of the most influential modelling parameters on emissions predictions. From the above text, it can be concluded that T_{IVC}, combustion chamber surface temperatures, interzonal mass transfer to zones 10 and 11, and their size are influential. Mass of LRF is included since the present model doesn't include a lambda controller on NG injector. Thus, m_{LRF} is a direct input and the changes in λ_{LRF} due cycle-to-cycle variations in mass of inducted air cannot be considered. Further, there is the fact of in-accuracies in measurements of fuel flow rate from experiment, which is used to obtain m_{LRF}. These parameters are listed in Table 5, and sensitivity analysis is conducted by introducing a + 1 % variation in these parameters above the baseline values of case B.

It can be observed that calibration of sizing of zones 11 and 12, and the interzonal mass transfer to them is important for UHC emissions, as shows sensitivity. Unsurprisingly, T_{IVC} has a big impact on the both emission's prediction, by increasing NO_X and reducing UHC. m_{LRF} has the largest impact on NO_X predictions, but negligible impact on UHC emissions. Furthermore, interzonal mass transfer to zones 11 and 12 has certain degree of impact on UHC results. In the analysis, it has been varied by multiplying a tuning factor over the value that is obtained from the turbulence model (section 2.2.2). Among combustion chamber surfaces, T_{liner} shows the biggest impact on both, with its influence begin slightly higher on NO_X than UHC.

Based on these results, UVATZ is calibrated towards emissions predictions. The first two parameters are globally calibrated since they are a characteristic of the model. A value of 0.45 and a factor of 1.3 is selected. For T_{IVC} and m_{LRF} required minor case dependent adjustment, wherein case B did not require any change. For case A and C, T_{IVC} and m_{LRF} had to be varied within 1 % and 3 % respectively. The combustion chamber surface temperatures where individually calibrated, with T_{liner} varied with ± 5 K, while T_{pist} and T_{head} varied within ± 20 K.

Results of the calibrated model is shown in Fig. 18, which was achieved without negatively impacting overall predictions of combustion performance. The data in the plots is normalized to experimental measurements of case B. It can be observed that emissions of UHC and NO_X demonstrate the correct trend with predictions within 35 % error limits to experimental measurement. The results of UHC predictions indicate a systematic error, i.e., overprediction.

Although this will be fixed with further fine-tuning, for the purposes of the current research, it suffices as a first showcase in demonstrating the capabilities of UVATZ. A potential measure for improving emissions accuracy is by calibrating the parameters Le, Pr_t and Sc_t, which are assumed unity (Section 2.2.2). Although they were excluded as governing assumptions of UVATZ, initial studies have shown that varying these parameters within a reasonable range (0.7 – 1.3) has an impact on emissions results without affecting the combustion performance. Another improvement strategy would be to employ predictive wall temperature model, as the one provided in GT-suite [47], wherein a finite-element solution of the temperature field is obtained for the cylinder, head and piston structures. This excludes the necessity of tuning T_{liner}, T_{pist} and T_{head}. A related strategy is coupling UVATZ to a 1D representation of air- and fuel-path, as in GT-suite, alleviating the need to tune T_{IVC} and m_{LRF}. All of these improvement strategies are under assessment in the follow-up work, within the context of extensive experimental campaign, as discussed in Section 5.2.

Table 5
Sensitivity analysis of model parameters on emission results; each model parameter is varied by + 1 % from the baseline value of case B.

Model parameter	NOx [%]	UHC [%]
zone size (11 + 12)	0.02	1.65
IZMT (11 + 12)	−0.02	−1.47
T_{IVC}	8.48	−4.83
m_{LRF}	13.29	−0.39
T_{liner}	2.82	−1.29
T_{pist}	0.94	0.40
T_{head}	0.78	−0.48

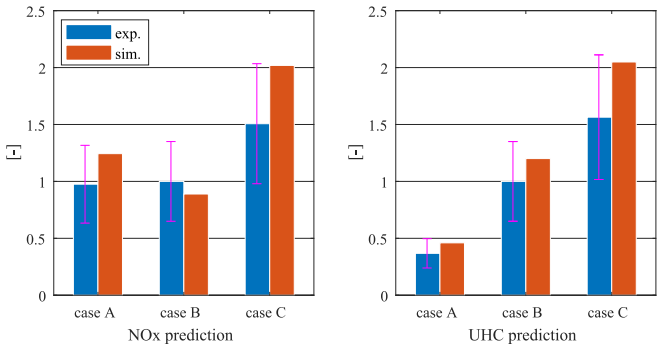

Fig. 18. Validation of simulated NO_X (left) and UHC (right) predictions against experimental measurements. Data in respective plots is normalised to the measured values NO_X and UHC from case B.

4. Discussion – Improvements on UVATZ

This section highlights the combined effect of the improvements made to UVATZ, as described in section 3. The discussions follow the establish research objectives for improvements in model autonomy and predictivity. The first part demonstrates the combined capabilities of the semi-predictive HRF stratification, *K-k* turbulence sub-model and emissions, via a parametric study of typical engine operating parameters. Although experimental validation is the preferred, the choice is driven by the limited availability of experimental data. Nevertheless, the objective of the parametric study is trend-wise verification with observations drawn from similar experimental investigation from literature. The second part of this section summaries the improvements by comparing against the baseline version of UVATZ in terms of accuracy and predictivity for all three operating points.

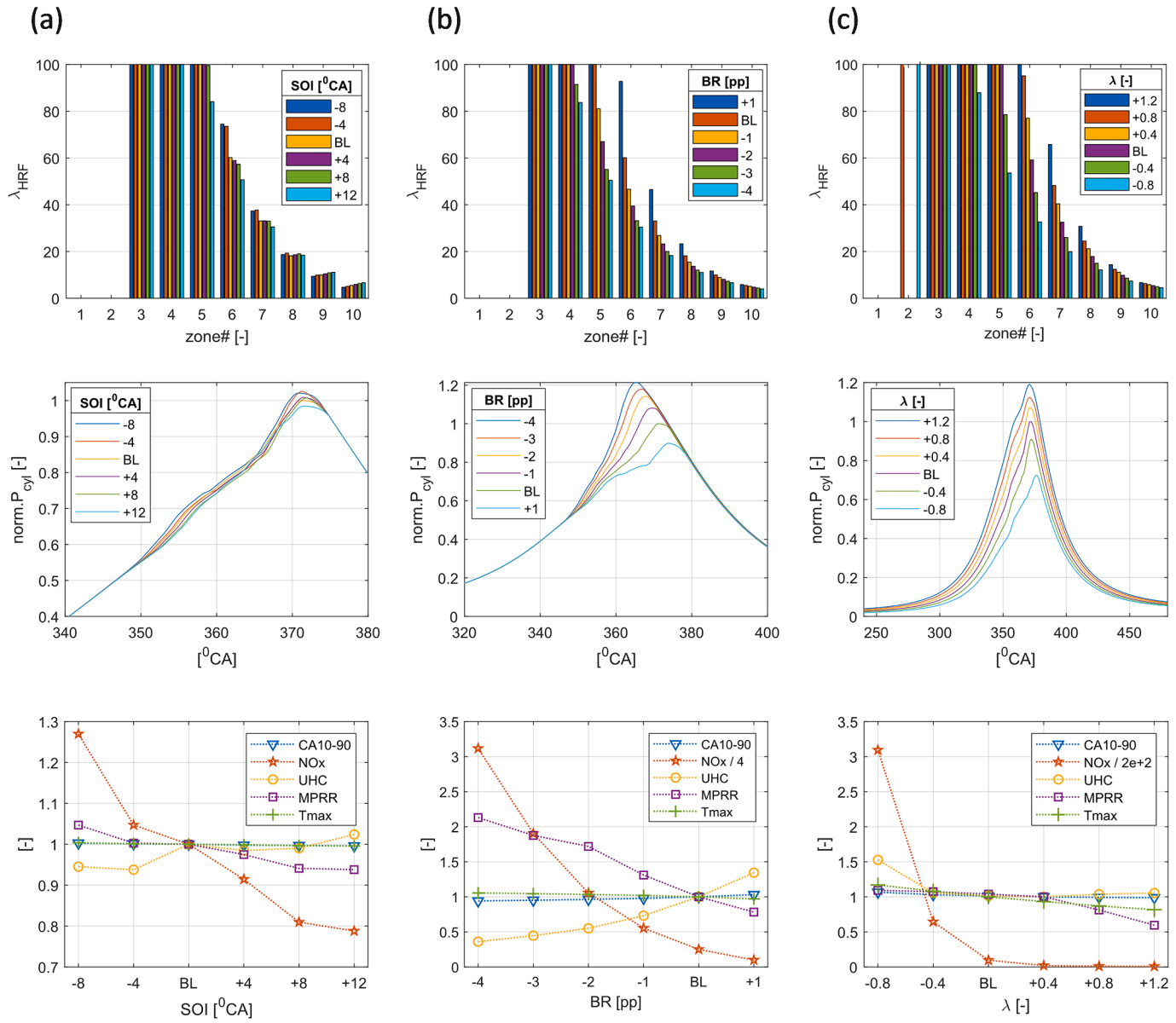

Fig. 19. Sweeps of (a) SOI – injection timing of diesel; (b) BR with fixed total fuel energy; (c) λ by varying boost pressure, about case B indicated as (BL). Top row shows the HRF stratification for each simulation case, while middle row shows the resulting pressure curve normalised to P_{max} of BL. Bottom row shows performance parameters normalised to BL values. NO_X results for (b) and (c) is additionally scaled as indicated in the legend.

4.1. Improved autonomy

Predictivity of the UVTATZ modelling framework with improvements including the physics-based *K-k* turbulence model and the predictive HRF stratification procedure, is assessed via parametric analysis. The scope is limited to the operating parameters of SOI, BR and the overall λ. The baseline (BL) conditions of case B are selected for the investigations. As such, SOI is swept within a range of 20°CA, BR within 5 pp and λ within 2. The variation in BR is obtained via mass of injected diesel in the cylinder, which is changed along with the amount of injected NG to keep the total fuel energy fixed at baseline. λ is varied based on change in boost pressure (P_{iman}). The simulations results are presented in Fig. 19. Worth noting that SOI is quantified with respect to crank angle before TDC.

Initialization of UVATZ with respect to the zonal HRF distribution for the sweeps obtained from the predictive HRF stratification procedure is shown in the first row of Fig. 19. For the SOI sweep it can be observed that as injection timing is advanced, HRF is increasingly seeded towards the middle zones (3–7). Specifically, ${}^{HRF}\lambda_{10}$ increases, while ζ_{∇} decreases with SOI. Observing the plot for BR sweep, HRF in the zones become increasingly leaner as BR increases, which naturally follows from the reduced quantity of diesel injected. For the sweep in λ, it can be observed that the zones become increasingly lean. This can be attributed phenomenologically to the increasing in-cylinder charge density, which decelerates the spray penetration rate in the radial direction, instead increasing break-up and air entrainment. As such, ${}^{HRF}\lambda_{10}$ including ζ_{∇} increases with P_{iman}.

From the pressure plots (2nd row) it can be observed that the sensitivity to SOI is comparatively small, with the P_{max} value decreasing at an average rate of 0.325 bar per °CA SOI. Further insights can be obtained from the last row, based on combustion characteristics and emissions. Maximum pressure rise rate (MPRR) shows minor sensitivity (negative slope) to SOI, but the trends in NO_x and UHC are noteworthy. NO_x shows a decreasing trend of 1.7 g/h per °CA SOI, while UHC displays an increase of 5.3 g/h per °CA SOI. This can be explained by a decrease in peak combustion temperature (T_{max}), which however changes at a small rate of 0.7 K per °CA SOI. Additionally, combustion duration (CA10-90) shortens by 0.25°CA per °CA SOI change. It is worth mentioning that combustion phasing (CA50) was delayed with advancing SOI, which however demonstrated a minor sensitivity (0.06°CA per °CA SOI), for which reason it is not shown.

For the BR sweep, injected diesel mass was varied at a rate of 17 % per pp BR. It can be observed that peak pressure reduces by nearly 3.1 bar per BR pp, with CA50 delayed by 2°CA per pp change in BR. This occurs due to the reduction in overall reactivity of the charge with BR, since amount of diesel injected reduces. Consequently, this explains the decreasing trend in MPRR and combustion temperature. The sensitivity observed for NO_x was larger than other quantities due to which it is scaled by 1/4 to fit in the plot (Fig. 19b 3rd row). As such, NO_X decreased at a rate of 42 g/h per pp change in BR, and UHC increased at a rate of 63 g/h per pp BR. In terms of percentage change relative to BL data, NO_X varies at a rate of −120 % per pp BR, while the rate for UHC is + 26 %.

Results for λ sweep are obtained by varying P_{iman} by 1.25 bar for unit change in λ. As such, in cylinder pressure increases, with a large change in peak value initially by + 75 bar per unit λ change, which then reduces to + 21.25 bar. From the bottom plot, it can be additionally inferred that while MPRR is relatively insensitive, it reduces during the latter part, for $\lambda > \lambda_{BL} + 0.8$. This is a consequence of increasing leaner combustion, indicated by the trend in T_{max}. As such, NO_x emission shows large sensitivity, and is scaled by 1/2e + 2. The decrease in NO_X is initially by 3000 % relative to BL, which later reduces to about 1 %. Similarly, the rate of change of UHC emission is initially –11 % relative to BL, which then changes in trend to + 0.7 %, when $\lambda > \lambda_{BL} + 0.8$. At such a large λ (given baseline setting of BR and SOI) T_{max} nears 1550 K, implying lowered combustion efficiency and increasing unburnt fuel.

The trends in performance parameters observed here can be corroborated with the experimental results of Doosje et al. [7], where a heavy-duty RCCI engine running on natural gas and single injection diesel strategy was studied. For low and part load conditions, results for sweep of SOI_{HRF} revealed that emissions of NO_X decrease, and that of UHC to increase, with advanced injection timing. Also, peak values of pressure and pressure rise rate shows increasing trend. These trends match with the presented simulation results. It is worth mentioning that in the experimental studies, the performance parameters displayed non-monotonic trend due to large range within with SOI was swept, −5 to −60°CA aTDC). However, the focus is constrained to < -40°CA for the purposes of the present analysis.

For the BR sweep, Doosje et al. studied blending > 85 %, which matches the present conditions. They observed that increasing BR, caused NO_X to decrease and UHC to increase. Although the trends match, the large sensitivity displayed by NO_X here was not observed in the experimental results. The authors also measured post turbine temperature, which revealed a slight decreasing trend. Although this is not the same as T_{max} illustrated here, it provides insight into the trend in average in-cylinder temperature. On the whole, while it is difficult to draw conclusions on the magnitude of sensitivity, the trends in results nonetheless, match with the simulations. Similar conclusions can be obtained following other investigations, for instance, the work of Nieman et al. [48].

4.2. Improved predictivity

Compared against the performance of the baseline version, Fig. 20 summarises the improvements in predictions. The parameters are those most relevant from a controller development perspective, i.e., CA50, IMEP, NO_X and UHC emissions. Also included are the CHR profiles normalized to total fuel energy of the respective cases, to provide insight to overall combustion performance.

An improvement in CA50 predictions is observed across all cases, by approximately 1°CA over the baseline model. As such, the accuracy in CA50 for the improved UVATZ is 1.55°CA on average. This is substantiated by the improvements in heat release rate predictions, which better matches the corresponding experimental trace, as included in Fig. 20. This stems from better prediction of the phase before CA20, and in latter phase, between CA60 and CA90. A delayed CA50 is observed in the baseline model version, despite which combustion rate accelerates during the latter phase, causing an overestimation in the duration CA50-80 by 5°CA. However, this error is drastically reduced to 0.8°CA in the improved UVATZ. Worth noting that the error in CA50 remains systematic in nature, and is associated to the employed chemical kinetics scheme.

According to Fig. 20, the error in IMEP720 on average is reduced from 3.5 % to 1.3 %. This is a consequence of better prediction of in-cylinder pressure with a decrease in its RMS error by 0.41 bar, and position of peak pressure improved by nearly 10°CA. Thus, the processed heat release is also predicted well, with a reduction in the RMS error of 245J. Additionally, predictions of NO_X and UHC are significantly improved in the upgraded UVATZ model. This is a consequence of emissions specific model calibration, as illustrated in the bar plot of UHC, where the predictions by the previous UVATZ model are off by 2–3 orders of magnitude, an error of 1500 %. Also, results of NOx are missing in the prior UVATZ model, since the unmodified Yao et al. [37] mechanism was employed. Ultimately, with the upgraded UVATZ model, predictivity within 35 % is achieved.

Finally, Fig. 21 also illustrates the simulation time required by both model versions for each case, averaged over three runs. It is worth noting that both models were executed on the same computing hardware, an 8th generation Intel® CORE i5 processor, on single core. The prior UVATZ version requires 2.4 min, while the improved model requires 3.9 min, which translates to a 67 % increase. The number of

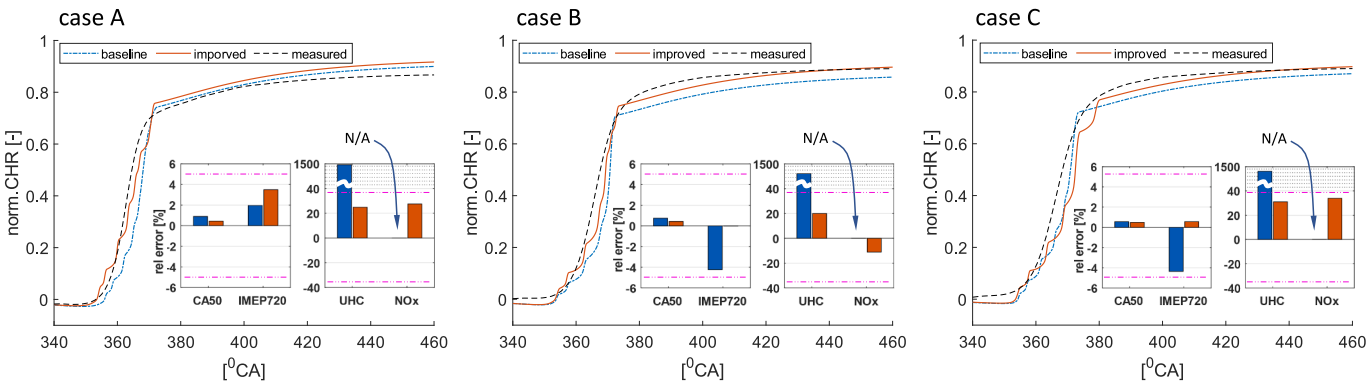

Fig. 20. Comparison of model predictivity of the improved version (red) against baseline version (blue) of UVATZ: pink dashed line indicates the target accuracy. The CHR traces are normalized to the total fuel energy of their respective cases.

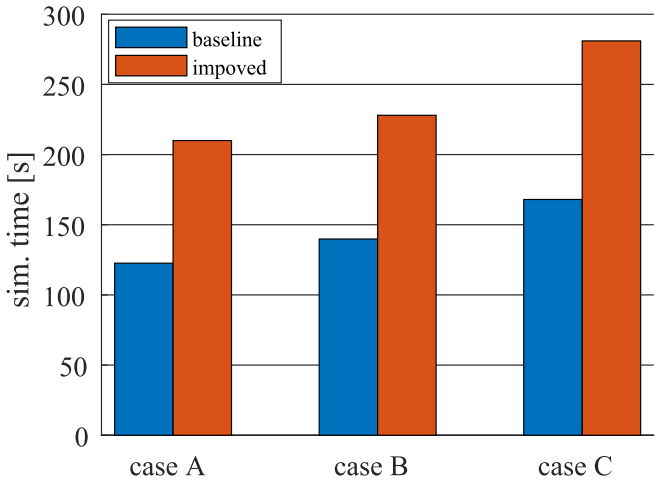

Fig. 21. Comparison of simulation time of the improved against baseline UVATZ model.

equations solved has increased (4 additional ODEs per zone for NO_X species, and 3 additional (explicit) ODEs for the *K-k* sub-model). The finer resolution of zones 11 and 12 (Fig. 14b) requires smaller time steps to resolve the interzonal flows, so this is also a contributing factor.

5. Conclusions and outlook

The UVATZ (University of Vaasa Advanced Thermo-kinetic multi-zone) model is developed in this study as a fully predictive, performance-oriented simulation tool for reactivity controlled compression (RCCI) engines. Built upon its initial realization [23] the present work advances the model's autonomy in terms of predicting high reactivity fuel (HRF) stratification via a semi-predictive approach, and interzonal mixing based on the physics of turbulent energy cascade. The CFD assisted calibration based on state-of-the-art experiments from a Wärtsilä 20DF engine demonstrates reproducibility of all the performance and emissions indicators across relevant operating parameter sweeps. The key highlights of this endeavour including future work are listed below.

5.1. Key takeaways

- Autonomy of UVATZ to operating parameters affecting HRF stratification is addressed by a response surface model (RSM) of HRF mass distribution profiles from CFD results. Induced by predictors of injection timing, mass of fuel and charge density, a feasibility analysis both within and outside the calibration envelope, showcases the potential of this simple approach in enabling UVATZ to reproduce the correct trends in engine performance indicators.
- Validation against CFD results demonstrates the ability of the 0D energy cascade turbulence model to reproduce the turbulent kinetic energy and turbulent viscosity within an accuracy of 10 % root mean square error. By virtue of its phenomenological basis, this sub-model enables UVATZ to reflect changes in engine performance due to in-cylinder flow variations resulting from engine operation, which is inadequately captured by the Yang and Martin approach.
- By employing a chemical-kinetics scheme of 58 species and 281 reactions, comprehensive validation of UVATZ demonstrates key combustion indicators within the target of 5 % error, with combustion phasing predicted $< 1.5°$CA. Outside the calibration envelope, the model's predictions including those of emissions correspond well (trend-wise) with similar experimental investigation.
- Dedicated calibration of UVATZ towards emissions, which include the interzonal heat and mass flow to the boundary zones and their thickness, demonstrates both nitrogen oxides and hydrocarbon emissions predicted within 35 % error to measurements, a first for this class of multizone models for RCCI combustion.
- Finally, these simulations are achieved with an average duration under 4 min per four-stroke cycle (based on an Intel® CORE i5 processor, utilizing single core)

5.2. Outlook

The ambition for the developed UVATZ is in its ultimate utility for rapid prototyping of next-generation marine engines. In the context of model-based development, the prior iteration of [23] UVATZ has already been used towards model predictive control development [49,50] and optimization [51] studies. The applications furthermore encompass engine-aftertreatment calibration [52], variable valve actuation and fuel blending studies, to name a few. This context is holistically illustrated in the graphical abstract. Such a development roadmap requires dedicated infrastructure, resources and strategic commitment, as governed within a portfolio of projects headed by the university of Vaasa which include Clean Propulsion Technologies [53], CASEMATE [54] and DAZE [55]. Towards this ultimate goal, the improvement points of UVATZ are:

- HRF stratification model: A more sophisticated RSM to account for curvature in the response due to a broad design space of the factors. This being facilitated by a more dense design of CFD simulations. An alternative is to exploit a 1D spray model for determining fuel stratification. Here, an approach similar to that of Ruth and O'Connor [56] is being currently explored.
- Emission predictivity: enabled by fine tuning the model parameters including *Le*, Pr_t and Sc_t. Furthermore, coupling UVATZ with GT-

suite to leverage the 1D air- and fuel-path models and finite-element based wall temperature prediction.
- Comprehensive validation: necessary to rigorously assess all modelling features over a broad dataset. To this end, an extensive experimental campaign on the W20 platform is being conducted under the framework of the aforementioned projects.
- Simulation speed: where a target of under one minute will be achieved via techniques such as advanced solvers [57–59], tabulated chemistry [20] and parallel computing.

Declaration of generative AI in scientific writing.

The authors declare that no generative AI and AI-assisted technologies were used in the writing process.

CRediT authorship contribution statement

Aneesh Vasudev: Writing – original draft, Visualization, Validation, Software, Methodology, Investigation, Funding acquisition, Formal analysis, Conceptualization. **Alireza Kakoee:** Writing – original draft, Visualization, Validation, Software, Methodology, Formal analysis, Data curation. **Martin Axelsson:** Writing – review & editing, Writing – original draft, Resources, Investigation, Data curation. **Hamidreza Maleki Almani:** Formal analysis. **Jari Hyvönen:** Writing – review & editing, Supervision, Resources. **Maciej Mikulski:** Writing – review & editing, Supervision, Resources, Project administration, Methodology, Funding acquisition, Conceptualization.

Declaration of competing interest

The authors declare that they have no known competing financial interests or personal relationships that could have appeared to influence the work reported in this paper.

Data availability

The data that has been used is confidential.

Acknowledgements

The work was conducted in the framework of the Clean Propulsion Technologies project with financial support from Business Finland (ref. 38485/31/2020). The authors also acknowledge the research grant from the Finnish Cultural Foundation (South Ostrobothnia Regional Fund) grant no. 10211786. Finally, we appreciate the invaluable contribution of Mr. David Wilcox in proofreading our manuscript and providing his expert suggestions on stylistic points.

References

[1] Paykani A, Garcia A, Shahbakhti M, Rahnama P, Reitz RD. Reactivity controlled compression ignition engine: Pathways towards commercial viability. Appl Energy 2021;282:116174. https://doi.org/10.1016/j.apenergy.2020.116174.
[2] Mikulski M, Ramesh S, Bekdemir C. Reactivity Controlled Compression Ignition for clean and efficient ship propulsion. Energy 2019;182:1173–92. https://doi.org/10.1016/j.energy.2019.06.091.
[3] Curran SJ, Hanson RM, Wagner RM. Reactivity controlled compression ignition combustion on a multi-cylinder light-duty diesel engine. Int J Engine Res 2012;13:216–25. https://doi.org/10.1177/1468087412442324.
[4] Inagaki K, Fuyuto T, Nishikawa K, Nakakita K, Sakata I. Dual-fuel PCI combustion controlled by in-cylinder stratification of ignitability. SAE International 2006. https://doi.org/10.4271/2006-01-0028.
[5] Benajes J, García A, Monsalve-Serrano J, Balloul I, Pradel G. Evaluating the reactivity controlled compression ignition operating range limits in a high-compression ratio medium-duty diesel engine fueled with biodiesel and ethanol. Int J Engine Res 2017;18:66–80. https://doi.org/10.1177/1468087416678500.
[6] Ganesan N, Le TH, Ekambaram P, Balasubramanian D, Le VV, Hoang AT. Experimental assessment on performance and combustion behaviors of reactivity-controlled compression ignition engine operated by n-pentanol and cottonseed biodiesel. J Clean Prod 2022;330:129781. https://doi.org/10.1016/j.jclepro.2021.129781.
[7] Doosje E, Willems F, Baert R. Experimental demonstration of RCCI in heavy-duty engines using diesel and natural gas. SAE International 2014. https://doi.org/10.4271/2014-01-1318.
[8] Dahodwala M, Joshi S, Koehler EW, Franke M. Investigation of diesel and CNG combustion in a dual fuel regime and as an enabler to achieve RCCI combustion. SAE International 2014. https://doi.org/10.4271/2014-01-1308.
[9] Paykani A, Kakaee A-H, Rahnama P, Reitz RD. Progress and recent trends in reactivity-controlled compression ignition engines. Int J Engine Res 2016;17:481–524. https://doi.org/10.1177/1468087415593013.
[10] Egüz U, Maes NCJ, Leermakers CAJ, Somers LMT, Goey LPHD. Predicting auto-ignition characteristics of RCCI combustion using a multi-zone model. Int J Automot Technol 2013;14:693–9. https://doi.org/10.1007/s12239-013-0075-2.
[11] Vasudev A, Mikulski M, Balakrishnan PR, Storm X, Hunicz J. Thermo-kinetic multi-zone modelling of low temperature combustion engines. Prog Energy Combust Sci 2022;91:100998. https://doi.org/10.1016/j.pecs.2022.100998.
[12] Bekdemir C, Baert R, Willems FPT, Somers LMT. Towards control-oriented modeling of natural gas-diesel RCCI combustion. SAE International 2015. https://doi.org/10.4271/2015-01-1745.
[13] Mikulski M, Bekdemir C. Understanding the role of low reactivity fuel stratification in a dual fuel RCCI engine – A simulation study. Appl Energy 2017;191:689–708. https://doi.org/10.1016/j.apenergy.2017.01.080.
[14] Indrajuana A, Bekdemir C, Luo X, Willems F. Robust multivariable feedback control of natural gas-diesel RCCI combustion. IFAC-PapersOnLine 2016;49:217–22. https://doi.org/10.1016/j.ifacol.2016.08.033.
[15] Indrajuana A, Bekdemir C, Feru E, Willems F. Towards model-based control of RCCI-CDF mode-switching in dual fuel engines. SAE International 2018. https://doi.org/10.4271/2018-01-0263.
[16] Mikulski M, Balakrishnan PR, Doosje E, Bekdemir C. Variable valve actuation strategies for better efficiency load range and thermal management in an RCCI engine. SAE International 2018. https://doi.org/10.4271/2018-01-0254.
[17] Mikulski M, Balakrishnan PR, Hunicz J. Natural gas-diesel reactivity controlled compression ignition with negative valve overlap and in-cylinder fuel reforming. Appl Energy 2019;254:113638. https://doi.org/10.1016/j.apenergy.2019.113638.
[18] Lashkarpour SM, Khoshbakhti Saray R, Najafi M. Multi-zone model for reactivity controlled compression ignition engine based on CFD approach. Energy 2018;156:213–28. https://doi.org/10.1016/j.energy.2018.05.084.
[19] Yang J, Martin JK. Approximate solution—One-dimensional energy equation for transient, compressible, low mach number turbulent boundary layer flows. ASMEJ Heat Transfer 1989;111:619–24. https://doi.org/10.1115/1.3250727.
[20] De Bellis V, Malfi E, Lanotte A, Fasulo G, Bozza F, Cafari A, et al. Development of a phenomenological model for the description of RCCI combustion in a dual-fuel marine internal combustion engine. Appl Energy 2022;325:119919. https://doi.org/10.1016/j.apenergy.2022.119919.
[21] Eichmeier JU, Reitz RD, Rutland C. A zero-dimensional phenomenological model for RCCI combustion using reaction kinetics. SAE Int J Engines 2014;7:106–19. https://doi.org/10.4271/2014-01-1074.
[22] Franken T, Matrisciano A, Sari R, Fogué Robles Á, Monsalve-Serrano J, Lopez PD. Modeling of reactivity controlled compression ignition combustion using a stochastic reactor model coupled with detailed chemistry. SAE International 2021. https://doi.org/10.4271/2021-24-0014.
[23] Vasudev A, Cafari A, Axelsson M, Mikulski M, Hyvönen J. Towards next generation control-oriented thermo-kinetic model for reactivity controlled compression ignition marine engines. SAE 2022. https://doi.org/10.4271/2022-01-1033.
[24] Kakoee A, Vasudev A, Smulter B, Hyvönen J, Mikulski M. A fully predictive 1-D modelling framework for reactivity-controlled compression ignition engine via chemistry based multi-zone model. SAE International 2023. https://doi.org/10.4271/2023-24-0001.
[25] Kee RJ, Coltrin ME, Glarborg P, Zhu H. Chemically reacting flow: theory, modeling and simulation. 2nd ed. NJ, USA: Wiley; 2017.
[26] Chang J, Güralp O, Filipi Z, Assanis D, Kuo T-W, Najt P, et al. New heat transfer correlation for an HCCI engine derived from measurements of instantaneous surface heat flux. SAE Transactions, Section 3: Journal of Engines 2004;113:1576–93.
[27] Imtenan S, Varman M, Masjuki HH, Kalam MA, Sajjad H, Arbab MI, et al. Impact of low temperature combustion attaining strategies on diesel engine emissions for diesel and biodiesels: A review. Energ Conver Manage 2014;80:329–56. https://doi.org/10.1016/j.enconman.2014.01.020.
[28] Kokjohn SL, Musculus MPB, Reitz RD. Evaluating temperature and fuel stratification for heat-release rate control in a reactivity-controlled compression-ignition engine using optical diagnostics and chemical kinetics modeling. Combust Flame 2015;162:2729–42. https://doi.org/10.1016/j.combustflame.2015.04.009.
[29] Kongsereeparp P, Kashani B, Checkel MD. A stand-alone multi-zone model for combustion in HCCI engines. Internal Combustion Engine Division Fall Technical Conference, Cannada: ASME 2005:265–74. https://doi.org/10.1115/ICEF2005-1241.
[30] Egüz U, Leermakers CA, Somers LM, de Goey LP. Premixed charge compression ignition combustion modelling with a multi-zone approach including inter-zonal mixing. Proceedings of the Institution of Mechanical Engineers, Part D: Journal of Automobile Engineering 2013;227:1313–24. https://doi.org/10.1177/0954407012474193.
[31] Bissoli M, Frassoldati A, Cuoci A, Ranzi E, Mehl M, Faravelli T. A new predictive multi-zone model for HCCI engine combustion. Appl Energy 2016;178:826–43. https://doi.org/10.1016/j.apenergy.2016.06.062.
[32] Komninos NP, Kosmadakis GM. Heat transfer in HCCI multi-zone modeling: Validation of a new wall heat flux correlation under motoring conditions. Appl Energy 2011;88:1635–48. https://doi.org/10.1016/j.apenergy.2010.11.039.

[33] Bozza F, Teodosio L, De Bellis V, Fontanesi S, Iorio A. A refined OD turbulence model to predict tumble and turbulence in SI engines. SAE Int J Engines 2019;12:15–30.
[34] De Bellis V, Bozza F, Fontanesi S, Severi E, Berni F. Development of a phenomenological turbulence model through a hierarchical 1D/3D approach applied to a VVA turbocharged engine. SAE Int J Engines 2016;9:514–27. https://doi.org/10.4271/2016-01-0545.
[35] Bozza F, Fontana G, Galloni E, Torella E. 3D–1D analyses of the turbulent flow field, burning speed and knock occurrence in a turbocharged SI engine. Consiglio Nazionale delle Ricerche 2007. https://doi.org/10.4271/2007-24-0029.
[36] Kim Y, Kim M, Oh S, Shin W, Cho S, Song HH. A new physics-based modeling approach for a 0D turbulence model to reflect the intake port and chamber geometries and the corresponding flow structures in high-tumble spark-ignition engines. Energies 2019;12. https://doi.org/10.3390/en12101898.
[37] Yao T, Pei Y, Zhong B-J, Som S, Lu T, Luo KH. A compact skeletal mechanism for n-dodecane with optimized semi-global low-temperature chemistry for diesel engine simulations. Fuel 2017;191:339–49. https://doi.org/10.1016/j.fuel.2016.11.083.
[38] Sun Y, Reitz R. Modeling diesel engine NOx and soot reduction with optimized two-stage combustion. SAE International 2006. https://doi.org/10.4271/2006-01-0027.
[39] Goodwin DG, Moffat HK, Cantera SRL. An object-oriented software toolkit for chemical kinetics. Thermodynamics And Transport Processes Version 230 Zenodo 2017. https://doi.org/10.5281/zenodo.170284.
[40] Cohen SD, Hindmarsh AC, Dubois PF. CVODE, A Stiff/Nonstiff ODE Solver in C. Comput Phys 1996;10:138. https://doi.org/10.1063/1.4822377.
[41] Kakoee A, Mikulski M, Vasudev A, Axelsson M, Hyvönen J, Salahi MM, et al. Start of injection influence on in-cylinder fuel distribution, engine performance and emission characteristics in a RCCI marine engine. Energies 2024;17(10):2370. https://doi.org/10.3390/en17102370.
[42] Musculus MPB. Multiple simultaneous optical diagnostic imaging of early-injection low-temperature combustion in a heavy-duty diesel Engine. SAE Transactions. SAE International 2006. https://doi.org/10.4271/2006-01-0079.
[43] Kokjohn S, Reitz RD, Splitter D, Musculus M. Investigation of fuel reactivity stratification for controlling PCI heat-release rates using high-speed chemiluminescence imaging and fuel tracer fluorescence. SAE Int J Engines 2012;5:248–69. https://doi.org/10.4271/2012-01-0375.
[44] Fogla N, Bybee M, Mirzaeian M, Millo F, Wahiduzzaman S. Development of a K-k-ϵ phenomenological model to predict in-cylinder turbulence. SAE Int J Engines 2017;10:562–75. https://doi.org/10.4271/2017-01-0542.
[45] Duan X, Lai M-C, Jansons M, Guo G, Liu J. A review of controlling strategies of the ignition timing and combustion phase in homogeneous charge compression ignition (HCCI) engine. Fuel 2021;285:119142. https://doi.org/10.1016/j.fuel.2020.119142.
[46] Čampara L, Hasanspahić N, Vujičić S. Overview of MARPOL ANNEX VI regulations for prevention of air pollution from marine diesel engines. SHS Web Conf 2018;58. Doi: 10.1051/shsconf/20185801004.
[47] GT-Power: Cooling Systems and Thermal Management Application Manual and Tutorial. Illinois, USA: Gamma Technologies LLC; 2023.
[48] Nieman DE, Dempsey AB, Reitz RD. Heavy-duty RCCI operation using natural gas and diesel. SAE Int J Engines 2012;5:270–85.
[49] Modabberian A, Storm X, Vasudev A, Zenger K, Hyvönen J, Mikulski M. Towards real-time combustion phase estimation for linear RCCI model-predictive control design. IFAC-PapersOnLine 2023;56:3170–7. https://doi.org/10.1016/j.ifacol.2023.10.1452.
[50] Storm X, Vasudev A, Shamekhi A-M, Modabberian A, Zenger K, Hyvönen J, et al. Real-time predictive model for reactivity controlled compression ignition marine engines. Control Eng Pract 2023;141:105724. https://doi.org/10.1016/j.conengprac.2023.105724.
[51] Brink A, da Silva PSP, Vasudev A, Mikulski M, Aro J, Hyvönen J. Heat-release shaping for optimal reactivity controlled compression ignition. 15th International Conference on Combustion Technologies for a Clean Environment. 2023.
[52] Kakoee A, Hunicz J, Mikulski M. Integrated 1D simulation of aftertreatment system and chemistry-based multizone RCCI combustion for optimal performance with methane oxidation catalyst. Journal of Marine Science and Engineering 2024;12. https://doi.org/10.3390/jmse12040594.
[53] Clean Propulsion Technology. Clean Propulsion 2021. https://cleanpropulsion.org/ (accessed August 12, 2021).
[54] CASEMATE - Computationally Aided Systems Engineering for Marine Advanced Technology for The Environment. University of Vaasa 2023. https://www.uwasa.fi/fi/tutkimus/hankkeet/casemate-computationally-aided-systems-engineering-marine-advanced-technology (accessed August 12, 2021).
[55] DAZE - Data Analytics for Zero Emission Marine. University of Vaasa 2023. https://www.uwasa.fi/en/research/projects/daze-data-analytics-zero-emission-marine (accessed August 12, 2021).
[56] Ruth D, O'Connor J. Development and verification of reduced-order model for diesel spray penetration and spreading during wall impingement. SAE 2017. https://doi.org/10.4271/2017-01-0814.
[57] McNenly MJ, Havstad MA, Aceves SM, Pitz WJ. Integration strategies for efficient multizone chemical kinetics models. SAE Int J Fuels Lubr 2010;3:241–55. https://doi.org/10.4271/2010-01-0576.
[58] Knoll DA, Keyes DE. Jacobian-free Newton-Krylov methods: a survey of approaches and applications. J Comput Phys 2004;193:357–97. https://doi.org/10.1016/j.jcp.2003.08.010.
[59] Wu H, Ma PC, Ihme M. Efficient time stepping for reactive turbulent simulations with stiff chemistry. 2018 AIAA Aerospace Sciences Meeting. American Institute of Aeronautics and Astronautics 2018. https://doi.org/10.2514/6.2018-1672.